Astronomy & Astrophysics

SiO outflows in the most luminous and massive protostellar sources of the southern sky

N. Guerra-Varas[1,2,3], M. Merello[1], L. Bronfman[1], N. Duronea[4,5], D. Elia[6], R. Finger[1], and E. Mendoza[7]

[1] Departamento de Astronomía, Universidad de Chile, Santiago, Chile
  e-mail: nguerra@ug.uchile.cl
[2] Dipartimento di Fisica, Università di Roma "Tor Vergata", Via della Ricerca Scientifica 1, 00133 Roma, Italy
[3] Department of Astronomy, University of Belgrade – Faculty of Mathematics, Studentski trg 16, 11000 Belgrade, Serbia
[4] Instituto de Astrofísica de La Plata (UNLP-CONICET), La Plata, Argentina
[5] Facultad de Ciencias Astronómicas y Geofísicas, Universidad Nacional de La Plata, Paseo del Bosque s/n, 1900, La Plata, Argentina
[6] INAF – IAPS, Via Fosso del Cavaliere, 100, 00133 Roma, Italy
[7] Dept. Ciencias Integradas, Facultad de Ciencias Experimentales, Centro de Estudios Avanzados en Física, Matemática y Computación, Unidad Asociada GIFMAN, CSIC-UHU, Universidad de Huelva, Spain

ABSTRACT

Context. High-mass star formation is far less understood than low-mass star formation. It entails the ejection of matter through molecular outflows, which disturbs the protostellar clump. Studying these outflows and the shocked gas caused by them is the key to a better understanding of this process.
Aims. The present study aims to characterise the behaviour of molecular outflows in the most massive protostellar sources in the southern Galaxy by looking for evolutionary trends and associating the presence of shocked gas with outflow activity.
Methods. We present APEX SEPIA180 (Band 5) observations (beamwidth ~36″) of SiO(4-3) molecular outflow candidates towards a well-selected sample of 32 luminous and dense clumps, which are candidates for harbouring hot molecular cores. We study the emission of the SiO(4-3) line, which is an unambiguous tracer of shocked gas, and recent and active outflow activity, as well as the HCO$^+$(2-1) and H^{13}CO$^+$(2-1) lines.
Results. Results show that 78% of our sample (25 sources) present SiO emission, revealing the presence of shocked gas. Nine of these sources are also found to have wings in the HCO$^+$(2-1) line, indicating outflow activity. The SiO emission of these nine sources is generally more intense ($T_a > 1$ K) and wider (~61 km s^{-1} FWZP) than the rest of the clumps with SiO detection (~42 km s^{-1} FWZP), suggesting that the outflows in this group are faster and more energetic. This indicates that the shocked material gets dispersed as the core evolves and outflow activity decreases. Three positive linear correlations are found: a weak one (between the bolometric luminosity and outflow power) and two strong ones (one between the outflow power and the rate of matter expulsion and the other between the kinetic energy and outflow mass). These correlations suggest that more energetic outflows are able to mobilise more material. No correlation was found between the evolutionary stage indicator L/M and SiO outflow properties, supporting that molecular outflows happen throughout the whole high-mass star formation process.
Conclusions. We conclude that sources with both SiO emission and HCO$^+$ wings and sources with only SiO emission are in an advanced stage of evolution in the high-mass star formation process, and there is no clear evolutionary difference between them. The former present more massive and more powerful SiO outflows than the latter. Therefore, looking for more outflow signatures such as HCO$^+$ wings could help identify more massive and active massive star-forming regions in samples of similarly evolved sources, and could also help identify sources with older outflow activity.

Key words. stars: formation – stars: massive – ISM: clouds – ISM: jets and outflows – ISM: molecules

1. Introduction

Massive stars are crucial to the evolution of the interstellar medium (ISM) and galaxies. However, they are difficult to observe and study because they are very scarce (about 1% of stellar populations), have short timescales and large heliocentric distances, and are embedded in very complex environments with high extinction and turbulence (e.g. Motte et al. 2018). Thus, high-mass star formation remains much less understood than low-mass star formation.

The current picture for high-mass star formation is that it takes place in massive dense cores (MDCs) embedded in massive clouds called massive star-forming (MSF) regions, and can be described by four main phases (van der Tak 2004; Motte et al. 2018; Elia et al. 2021; Urquhart et al. 2022; Jiao et al. 2023). Initially, in the quiescent or starless phase, the clump has no embedded objects and is not visible at 70 µm. Later, in the young stellar object (YSO) phase, the clump has warmed up enough to be detected at 70 µm. In this stage, (~10^4 yr), there is an embedded cold and collapsing prestellar core. When a protostar appears (protostellar phase, ~3 × 10^5 yr), it feeds on inflow material and its mass increases until it becomes a high-mass protostar. Within this phase, the hot molecular core (HMC) stage can be identified. Then, as the protostar evolves and its temperature increases, it starts emitting ultraviolet (UV) radiation, which quickly ionises the surrounding gas. This starts the ultra-compact (UC) HII region phase (~10^5–10^6 yr).

Massive star formation entails a greatly relevant feedback process: molecular outflows and jets (i.e. matter expulsion at high velocities due to angular momentum conservation during matter accretion; Arce et al. 2007; Bally 2016; Motte et al. 2018). This feedback process occurs throughout the whole of the high-mass formation process (Li et al. 2020; Yang et al. 2022; Urquhart et al. 2022), and outflow features have been used as an indication of massive star formation activity (Li et al. 2019c; Liu et al. 2020). In order to understand how massive stars form, the study of molecular outflows in MSF regions is imperative.

The study of outflows heavily depends on the tracer used. There is no such thing as a perfect outflow tracer (Bally 2016). However, the SiO molecule has been found to be a very good tracer of outflow activity and shocked material, and has been broadly used for this purpose (e.g. Beuther et al. 2002; López-Sepulcre et al. 2011; Bally 2016; Li et al. 2019b; Liu et al. 2021a,b, 2022; De Simone et al. 2022). Silicon falls onto the icy mantles of the dust grains of the ISM. When hit by shocks of gas, the dust grains can sublimate to the gaseous state, releasing the Si. Thus, the Si in the gas phase can react with oxygen to form SiO, making it observable in the millimetre (mm), sub-mm, and centimetre (cm) regimes via its rotational transitions (Schilke et al. 1997; Klaassen & Wilson 2007; Gusdorf et al. 2008). Unlike other molecules, SiO has a key advantage. Its emission is not easily contaminated by excited ambient material, which makes it an unambiguous tracer of shocked material, and thus of outflow activity. Studying SiO emission can shed light on the kinematics of outflows and on the relevant chemical processes that occur in shock environments, such as the formation of complex organic molecules (COMs; Bally 2016; Li et al. 2020; Rojas-García et al. 2022). Broad spectral width SiO emission (full width zero power, FWZP $\geq$ 20 km s^{-1}) and narrow spectral width SiO emission (FWZP $\leq$ 10 km s^{-1}) have both been observed (Garay et al. 2010; Leurini et al. 2014; Bally 2016; Csengeri et al. 2016; Li et al. 2019b; Zhu et al. 2020). It is thought that broad-width emission is due to high-velocity collimated shocks, while narrow-width emission is associated with less collimated low-velocity shocks, such as cloud-cloud collisions. It is possible to identify wings in the SiO spectral profile when it has a broad width, which are manifestations of SiO outflows. These have been extensively studied (Beuther et al. 2002; Liu et al. 2021a,b). Moreover, SiO outflow activity has been found to decrease and become less collimated over time (Arce et al. 2007; Sakai et al. 2010; López-Sepulcre et al. 2011). However, there is currently no consensus on whether SiO abundance decreases over time (Csengeri et al. 2016; Li et al. 2019b; Liu et al. 2022), and some works even conclude that SiO emission is much harder to interpret than just as a shock tracer (Widmann et al. 2016).

Another very helpful outflow tracer is HCO$^+$ emission (Myers et al. 1996; Rawlings et al. 2004; Klaassen & Wilson 2007; Bally 2016; Li et al. 2019a; Liu et al. 2020; He et al. 2021). This species traces the surrounding material of protostar regions (Rawlings et al. 2004) and traces the disk material in low-mass star formation (Dutrey et al. 1997). This species can trace both inflow and outflow motions (Klaassen & Wilson 2007). When outflows are strong enough, they can be observed in broad high-velocity wings in the spectral profile (Wu et al. 2005; He et al. 2021). When HCO$^+$, and other species such as CO, are dragged outwards due to the outflow, their spectral profiles present wings. This is caused by the greater velocity gradient of the dragged material. However, the spectral profile of this species experiences significant absorption, which often complicates its analysis. Moreover, studying the emission of

an HCO$^+$ isotopologue, H^{13}CO$^+$, can help distinguish between outflows and ambient dense gas as it traces dense gas only (see Sect. 3.1).

SiO line emissions are associated with recent and active outflow of matter, as shock chemistry processes happen in 10^2–10^4 yr, whilst the HCO$^+$ wing observations are associated with old 'fossil' outflows (Arce et al. 2007; Klaassen & Wilson 2007; López-Sepulcre et al. 2016; Li et al. 2019a). The detection of only one of these phenomena is enough to indicate the presence of a molecular outflow. If both are detected, then it is possible to confirm without ambiguity that there is ongoing matter expulsion (Klaassen & Wilson 2007). Outflows are associated with an advanced stage of evolution. If a molecular core does not have an outflow, it may be because it has not reached this point yet. However, it is also possible that it has already experienced a significant loss of material and/or that accretion and outflow activity have ceased.

In this work we present SiO(2-1), HCO$^+$(2-1), and H^{13}CO$^+$(2-1) APEX Band 5 observations towards a well-selected sample of 32 very massive and luminous protostellar sources that are amongst the brightest clumps in the Southern Milky Way. This study addresses several research questions, including how SiO outflows behave in the most massive protostellar sources, whether the presence of shocked gas is associated with outflow activity, and what different outflow signatures can tell us about similarly evolved sources.

This paper is organised as follows. In Sect. 2 we describe the studied sample, the selection criteria, and the observations. In Sect. 3 we analyse the data and describe how outflow and SiO detections were analysed. In Sect. 4 we calculate the outflow properties of the clumps and the SiO emission. In Sect. 5 we present relevant correlations, carry out a cross-check between SiO and outflow detections, and discuss possible evolutionary trends. Finally, in Sect. 6 we provide a summary of our main results and present our conclusions.

2. Observations

2.1. Source selection

The studied sample consists of 32 protostellar clumps (HMC candidates) from the Hi-GAL catalogue of compact sources (Elia et al. 2021), associated with CS(2-1) line emission from IRAS PSC sources with far-infrared colours of Ultra Compact HII regions by Bronfman et al. (1996). Their characteristics are presented in Table 1; the sources flagged with a black diamond (♦) have saturated Hi-GAL observations (see Appendix A). The sources have been given an identifier consisting of 'HC' (hot core) plus a number, and are listed in increasing order for convenience. The sources were selected using the following criteria:

1. Kinematic distance <6 kpc (from Reid et al. 2009; Hi-GAL distances were not used; see Appendix B);
2. Strong CS emission (Bronfman et al. 1996): Main-beam temperature in CS T_{MB}(CS) $\geq$ 1.5 K;
3. Surface density above the threshold for the formation of massive stars: Σ > 0.2 g cm^{-2} (e.g. Butler & Tan 2012; Merello et al. 2018);
4. Mass >100 $M_\odot$ (Elia et al. 2021);
5. High luminosity-to-mass ratio L/M. Values of this evolutionary stage indicator higher than 1 are associated with internal protostellar heating and the appearance of new stars in massive clumps (López-Sepulcre et al. 2011; Molinari et al. 2016).

Table 1. Studied sample sources.

Source	Hi-GAL name	IRAS name	α (J2000.0)	δ (J2000.0)	D (kpc)	V_{LSR}(CS) (km s^{-1})
HC01	HIGALBM5.6373+0.2352	17545-2357	17:57:35.0328	−23:58:08.472	2.95	9.1
HC02 ♦	HIGALBM5.8856-0.3920	17574-2403	18:00:30.4080	−24:03:59.663	2.94	9.3
HC03	HIGALBM6.7951-0.2571	17589-2312	18:01:57.7152	−23:12:34.844	3.56	21.1
HC04 ♦	HIGALBM10.4631+0.0298	18056-1952	18:08:36.5496	−19:52:14.534	5.29	68.9
HC05	HIGALBM12.8892+0.4895	18089-1732	18:11:51.4224	−17:31:27.620	2.88	33.8
HC06	HIGALBM12.9083-0.2603	18117-1753	18:14:39.5184	−17:52:00.710	2.96	36.6
HC07	HIGALBM16.5849-0.0505	18182-1433	18:21:09.0672	−14:31:49.184	3.84	59.1
HC08	HIGALBM301.1365-0.2259	12326-6245	12:35:35.1552	−63:02:32.633	4.31	−39.4
HC09	HIGALBM309.9212+0.4781	13471-6120	13:50:42.2184	−61:35:12.466	5.35	−58.4
HC10	HIGALBM311.6269+0.2898	14013-6105	14:04:55.0536	−61:20:07.120	4.57	−56.2
HC11	HIGALBM312.1074+0.3094	14050-6056	14:08:41.9400	−61:10:42.391	3.60	−48.4
HC12	HIGALBM317.4080+0.1102	14453-5912	14:49:07.8000	−59:24:45.623	2.69	−39.9
HC13	HIGALBM323.4594-0.0789	15254-5621	15:29:19.5696	−56:31:21.918	4.09	−67.5
HC14	HIGALBM326.7806-0.2411	15450-5431	15:48:55.2096	−54:40:38.525	3.87	−64.7
HC15	HIGALBM327.3918+0.1996	15464-5348	15:50:18.4992	−53:57:05.612	5.05	−88.6
HC16 ♦	HIGALBM330.8814-0.3656	16065-5158	16:10:20.4504	−52:05:56.908	3.77	−62.2
HC17	HIGALBM331.2786-0.1883	16076-5134	16:11:26.7480	−51:41:56.044	4.88	−87.7
HC18	HIGALBM332.2951-0.0938	16119-5048	16:15:45.4104	−50:55:54.512	3.17	−48.4
HC19	HIGALBM332.5443-0.1226	16132-5039	16:17:01.2000	−50:46:46.643	3.10	−46.7
HC20 ♦	HIGALBM333.1246-0.4244	16172-5028	16:20:58.1904	−50:35:19.190	3.33	−51.2
HC21	HIGALBM335.5848-0.2894	16272-4837	16:30:58.5120	−48:43:52.183	3.22	−46.6
HC22	HIGALBM339.6221-0.1209	16424-4531	16:46:06.1080	−45:36:44.003	2.60	−33.2
HC23	HIGALBM340.2740-0.2098	16452-4504	16:48:53.3160	−45:10:20.420	2.78	−45.5
HC24	HIGALBM341.1268-0.3456	16489-4431	16:52:33.2568	−44:36:10.613	2.72	−40.6
HC25	HIGALBM342.0590+0.4212	16489-4318	16:52:32.8656	−43:23:45.553	4.63	−71.0
HC26	HIGALBM342.7076+0.1257	16524-4300	16:56:03.1296	−43:04:43.489	2.74	−41.9
HC27	HIGALBM345.0035-0.2239	17016-4124	17:05:11.1168	−41:29:05.665	2.82	−26.6
HC28	HIGALBM350.0154+0.4332	17143-3700	17:17:45.4032	−37:03:11.642	3.87	−31.5
HC29	HIGALBM350.1024+0.0805	17160-3707	17:19:27.3216	−37:11:05.788	5.54	−69.5
HC30	HIGALBM351.0412-0.3354	17204-3636	17:23:50.2800	−36:38:57.138	2.70	−18.0
HC31	HIGALBM352.3155-0.4422	17244-3536	17:27:48.6096	−35:39:11.207	1.33	−10.8
HC32	HIGALBM354.6619+0.4800	17271-3309	17:30:22.6008	−33:11:17.668	3.73	−20.9

Although low-mass star-forming clumps may also have a high value of L/M, the lower limit set on the mass of the clump together with a high L/M ensures our sample will only consist of massive protostellar clumps.

The sources in our sample are at an advanced stage of evolution, either in the protostellar or compact HII region phase. A histogram of the luminosity-to-mass ratio L/M, which acts as an evolutionary stage indicator, is presented in Fig. 1 (see Table 1). The parameter L/M has a minimum value of 3 $L_\odot/M_\odot$, a maximum of 154 $L_\odot/M_\odot$, a mean of 45 $L_\odot/M_\odot$, and a median of 30 $L_\odot/M_\odot$.

The sources are very energetic, with bolometric luminosities up to $\sim 2.3 \times 10^5 L_\odot$. The selection criteria of the sources allowed us to work only with luminous, strong, and relatively near clumps. They are among the most luminous sources in the southern sky, and some of them have been extensively studied (see Appendix C). The continuum dust properties of the sources are shown in Table 2; the sources flagged with a black diamond (♦) have saturated Hi-GAL observations (see Appendix A) and were obtained from a SED fit (Elia et al. 2021). Compared with the general population of Hi-GAL protostellar sources (Elia et al. 2017, 2021), we see that our sample is much more massive and luminous. The median value for H$_2$ mass derived from dust M_{dust} and bolometric luminosity L_{Bol} for

our sample is 828 $M_\odot$ and 19839 $L_\odot$, respectively, whilst for Hi-GAL protostellar sources these values are equal to 464 $M_\odot$ and 1071 $L_\odot$, respectively. In comparison with the rest of the Hi-GAL sources within 6 kpc, the contrast is even greater since the mean bolometric luminosity is 206 $L_\odot$ and the mean dust mass is 88 $M_\odot$ in this region of the Galaxy. Finally, Fig. 2 shows the distribution in the Galactic plane of the sources presented in this work.

2.2. APEX observations

Observations were made using the SEPIA180 instrument at the Atacama Pathfinder Experiment (APEX)[1] in the Atacama Desert in Chile (Belitsky et al. 2018) for ten nights between November 2018 and October 2019. The observations were made in single-pointing mode. For each source a region free from emission was taken as reference from the dust maps at 250 μm by *Herschel*, typically at 300−500″ from the source. The system temperature was 174.30 K on average.

The band was tuned at 172 GHz in the LSB to observe the H^{13}CO$^+$(2-1) (173.507 GHz) and SiO(4-3) (173.688 GHz) lines,

---

[1] https://www.apex-telescope.org/ns/instruments/sepia/sepia180/
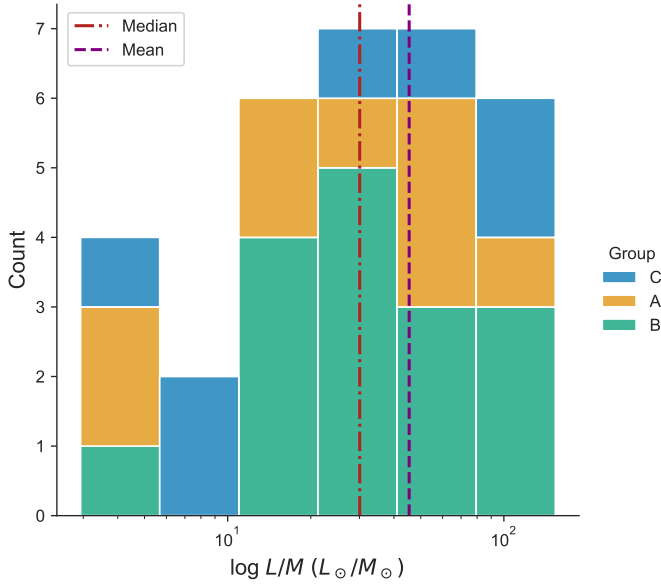
Fig. 1. Histogram of the luminosity-to-mass ratio L/M in logarithmic scale. The red and purple vertical lines denote the median (30 $L_\odot/M_\odot$) and the mean (45 $L_\odot/M_\odot$), respectively. Groups A, B, and C are defined in Table 6.
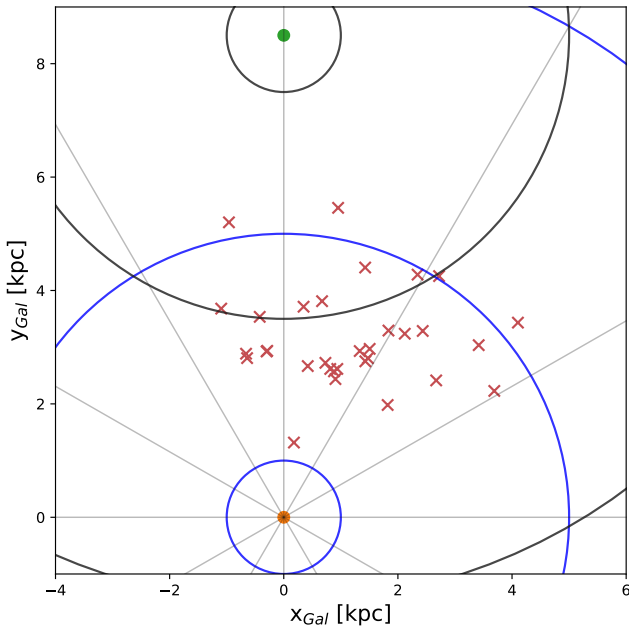
Fig. 2. Galactic distribution of the sources. The orange point corresponds to the Sun and the green point to the Galactic centre. The red crosses are the sources studied in this paper. The blue circles are centred on the Sun and the black circles on the Galactic centre. They indicate the 1, 5, and 10 kpc distances.

and centred at the HCO$^+$(2-1) line (178.375 GHz). The spectral resolution used was of $\Delta V = 0.2$ km s^{-1}, which gives a typical RMS noise temperature of 25 mK, and the main beam efficiency η_{MB} was equal to 0.83. APEX observations have an antenna temperature uncertainty of about 20% (APEX staff, priv. comm.). The frequency of the transitions used was obtained from the SPLATALOGUE[2] database. This frequency range corresponds to Band 5 of the Atacama Large Millimeter/submillimeter Array.

---

[2] https://splatalogue.online//advanced1.php

Table 2. Clump properties.

Source	L_{bol} ($10^3 L_\odot$)	M_{dust} ($M_\odot$)	T_{dust} (K)	L/M ($L_\odot/M_\odot$)
HC01	11.14	394.0	25.8	28.0
HC02 ♦	16.75	2017.0	25.0	72.0
HC03	20.57	1141.0	23.1	18.0
HC04 ♦	0.77	8675.0	25.0	25.0
HC05	22.04	540.0	33.4	41.0
HC06	42.28	1328.0	22.6	32.0
HC07	17.47	535.0	31.5	33.0
HC08	227.44	2803.0	33.5	81.0
HC09	222.95	1477.0	34.4	151.0
HC10	121.44	1458.0	30.4	83.0
HC11	68.39	701.0	25.6	98.0
HC12	2.70	785.0	18.3	3.0
HC13	142.72	929.0	31.5	154.0
HC14	8.67	799.0	19.4	11.0
HC15	13.55	1074.0	22.9	13.0
HC16 ♦	56.05	1962.0	25.0	3.0
HC17	100.00	1400.0	32.0	71.0
HC18	14.98	949.0	22.4	16.0
HC19	2.22	756.0	18.8	3.0
HC20 ♦	114.35	4980.0	25.0	3.0
HC21	19.10	1608.0	23.3	12.0
HC22	13.86	321.0	24.1	43.0
HC23	4.19	341.0	33.4	12.0
HC24	6.12	390.0	20.0	16.0
HC25	23.05	1001.0	23.2	23.0
HC26	24.66	585.0	28.8	42.0
HC27	67.66	1030.0	34.0	66.0
HC28	33.62	230.0	40.0	146.0
HC29	162.23	2083.0	27.5	78.0
HC30	11.50	456.0	27.0	25.0
HC31	4.56	105.0	25.9	43.0
HC32	6.34	859.0	20.6	7.0

The beam angular size can be calculated with the frequency f of a spectral line with $\theta'' = 7.8'' \times 800/f$. For these observations this results in a beam angular size of approximately 36″.

The CLASS software from the GILDAS[3] software package was used to reduce the spectra. It is used to process single-dish spectra and is oriented towards the processing of a large number of spectra. For every spectral line, the baseline was subtracted at first order and then centred to the V_{LSR} of the corresponding source.

3. Analysis

The SiO(4-3), H^{13}CO$^+$(2-1), and HCO$^+$(2-1) spectral profiles of source HC02 are presented in Fig. 3 as an example, where the red dotted line is at FWZP and the blue line in the H^{13}CO$^+$ panel shows the Gaussian fit (see Figs D.1–D.31 for the rest).

Results for the HCO$^+$(2-1), H^{13}CO$^+$(2-1), and SiO(4-3) spectral lines are displayed in Tables 3–5, respectively. We calculated the spatial beam size R with the angular beam size θ and distance to the source D:

$$R \text{ (pc)} = \theta\,('') \cdot D \text{ (pc)} \cdot \frac{\pi}{180} \frac{1}{3600}. \tag{1}$$

---

[3] https://www.iram.fr/IRAMFR/GILDAS/
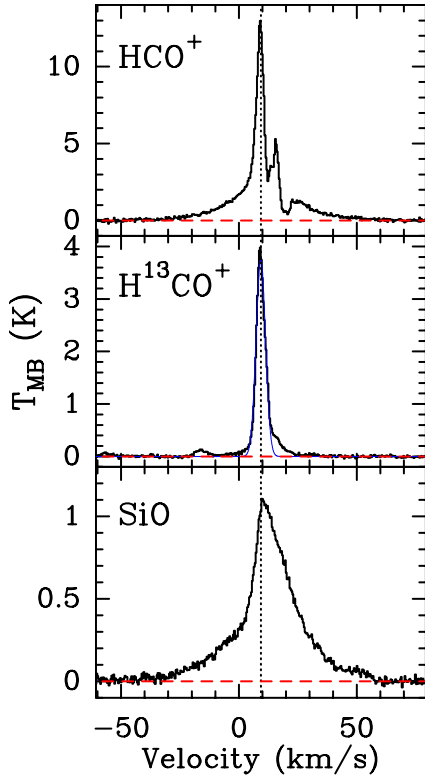
Fig. 3. Spectral profiles for source HC02, Group A. The red dotted line is at FWZP and the blue line in the H^{13}CO$^+$ panel shows the Gaussian fit.

Table 3. HCO$^+$ spectral line data.

Source	RMS (K)	Area (K km s^{-1})	FWZP (km s^{-1})	Peak T_{MB} (K)	Wings
HC01	0.04	11.9	23.97	2.73	
HC02	0.10	124.7	92.12	13.00	✓
HC03	0.09	11.7	19.86	2.35	
HC04	0.10	50.8	29.45	4.74	
HC05	0.11	7.3	19.86	2.15	
HC06	0.11	25.5	46.58	2.37	✓
HC07	0.12	16.1	16.10	4.52	
HC08	0.03	61.4	53.43	6.83	✓
HC09	0.03	13.9	26.37	3.29	
HC10	0.03	6.4	27.06	2.17	
HC11	0.03	5.1	18.84	1.24	
HC12	0.04	9.0	19.86	2.49	
HC13	0.05	28.7	27.06	5.74	
HC14	0.03	17.3	28.13	4.12	
HC15	0.02	24.8	31.17	3.46	
HC16	0.02	44.2	55.82	4.58	✓
HC17	0.03	23.7	53.77	2.20	✓
HC18	0.04	11.4	40.75	2.02	✓
HC19	0.05	8.3	10.96	2.55	
HC20	0.05	104.3	45.89	11.14	✓
HC21	0.05	45.2	35.27	9.37	✓
HC22	0.09	17.8	23.29	3.32	
HC23	0.03	17.0	27.06	3.25	
HC24	0.04	9.8	19.18	2.67	
HC25	0.05	4.6	19.52	1.21	
HC26	0.03	21.5	20.21	5.43	
HC27	0.04	20.1	52.40	2.44	✓
HC28	0.02	15.5	24.66	2.28	
HC29	0.02	33.3	29.45	4.51	
HC30	0.03	19.3	28.08	4.11	
HC31	0.03	14.4	14.73	2.88	
HC32	0.03	12.4	20.20	3.45	

It should be noted that since our observations do not resolve the singular clump, the spatial beam size is diluted and introduces uncertainties. We compared the beam size of the sources at the H^{13}CO$^+$(2-1) line with their beam-deconvolved sizes measured at 250 μm continuum emission obtained from the Hi-GAL catalogue of compact sources (Elia et al. 2021). The H^{13}CO$^+$ line traces the cold surrounding material; on the other hand, the cold dust is expected to emit at around 250 μm (i.e. they trace mostly the same dense gas; e.g. Elia et al. 2017). Thus, we computed the ratio of the clump sizes in 250 μm to those in the H^{13}CO$^+$(2-1) line. This indicates how beam dilution affects our results. We found that the beam size in our APEX observations is on average 2.35 times larger than the size of the clump at 250 μm. On the other hand, the SiO(4-3) line has an angular resolution of 36″, which corresponds to 0.087 pc at a distance of 1 kpc. The distances to our sources range from 1.33 to 5.54 kpc. These uncertainties propagate linearly to the column densities to be calculated in Sect. 4.1.2.

3.1. Clump tracer emission

The HCO$^+$ and H^{13}CO$^+$ species are commonly used as dense gas tracers. They are treated as linear rigid rotors (Mladenović 2017) and are expected to present a Gaussian profile. Although they are isotopologues, these lines present different behaviours. At a kinetic temperature of 20 K, the HCO$^+$(2-1) and H^{13}CO$^+$(2-1) lines have optically thin critical densities of 4.2×10^5 cm^{-3} and 3.8×10^5 cm^{-3} and effective excitation densities of 1.7×10^3 cm^{-3} and 7.1×10^4 cm^{-3}, respectively (Shirley 2015). The HCO$^+$ has a much lower effective density than its isotopologue, which indicates that HCO$^+$ traces regions with lower density, such as outflows and jets, which are usually less dense than the surrounding material. This is why HCO$^+$ traces both outflows and the surrounding material, whilst H^{13}CO$^+$ only traces the latter. The differences between these two lines are visually clear in their spectral profiles (see Fig. 3 and Appendix D). HCO$^+$ emission experiences significant absorption and self-absorption (Klaassen & Wilson 2007), and thus it is not possible to quantify properties of the clump using this spectral profile only. In addition, H^{13}CO$^+$ emission is optically thin and does not present absorption. Therefore, the Gaussian parameters fitted to the H^{13}CO$^+$(2-1) spectral profiles were used to calculate the properties of the cores for all the sources, and the velocity of the H^{13}CO$^+$(2-1) Gaussian peak was used to centre the standard of rest velocity V_{LSR} of the sources. The parameters of the HCO$^+$(2-1) spectral lines are displayed in Table 3, and the results from the Gaussian fit to the H^{13}CO$^+$(2-1) spectral profile are displayed in Table 4.

We note that if the outflow is strong enough, it is possible that the H^{13}CO$^+$ line presents wings as well, as is the case for source HC20 (see Fig. D.19). Since the sources in our sample are extreme, it is reasonable to see this feature. The wings in the H^{13}CO$^+$ line are much smaller than those in the HCO$^+$ line, and it is still possible to properly fit a Gaussian curve.

Since wings in the HCO$^+$ spectral profile are a very good indicator of outflows, its (2-1) spectral line was used to determine the presence of molecular outflows through the detection

Table 4. $H^{13}CO^+$ spectral line data.

Source	R (pc)	RMS (K)	Area (K km s^{-1})	Width (km s^{-1})	Position (km s^{-1})	Peak T_{MB} (K)
HC01	0.26	0.02	2.4	2.29	8.4	1.00
HC02	0.26	0.03	18.7	4.68	9.3	3.75
HC03	0.31	0.02	3.9	2.83	21.0	1.29
HC04	0.46	0.03	7.5	7.09	66.8	0.99
HC05	0.25	0.02	4.0	3.80	33.1	0.99
HC06	0.26	0.02	7.0	3.91	37.3	1.67
HC07	0.33	0.02	2.9	3.23	59.5	0.84
HC08	0.38	0.01	6.8	4.58	−39.5	1.40
HC09	0.47	0.02	3.8	3.09	−57.9	1.16
HC10	0.40	0.02	4.4	3.19	−54.9	1.30
HC11	0.31	0.01	1.3	2.96	−48.1	0.43
HC12	0.23	0.02	1.8	1.99	−40.2	0.86
HC13	0.36	0.03	4.2	2.94	−68.0	1.34
HC14	0.34	0.03	1.6	2.52	−64.9	0.59
HC15	0.44	0.03	3.1	3.80	−88.7	0.77
HC16	0.33	0.03	5.8	4.40	−62.7	1.24
HC17	0.425	0.03	4.0	4.60	−87.8	3.84
HC18	0.28	0.03	2.8	2.99	−48.5	0.88
HC19	0.27	0.03	1.1	1.67	−47.0	0.60
HC20	0.29	0.03	22.4	5.48	−53.2	3.84
HC21	0.28	0.02	7.8	3.54	−46.6	2.07
HC22	0.23	0.02	2.7	2.44	−34.3	1.04
HC23	0.24	0.01	2.8	2.85	−46.2	0.92
HC24	0.24	0.02	1.9	2.23	−40.8	0.78
HC25	0.40	0.01	2.2	4.19	−71.0	0.48
HC26	0.24	0.02	4.1	3.04	−40.8	1.27
HC27	0.25	0.02	7.4	6.30	−27.0	1.10
HC28	0.34	0.01	2.6	3.74	−31.5	0.65
HC29	0.48	0.01	5.1	3.72	−69.4	1.28
HC30	0.24	0.01	3.8	3.09	−18.0	1.16
HC31	0.12	0.01	4.1	3.05	−10.6	1.27
HC32	0.325	0.01	1.1	2.30	−20.5	0.44

of wings. In the literature, spectral lines with wings are usually modelled by a Lorentz distribution. However, this line presents significant absorption in our data, which makes any curve fit far too inaccurate. Thus, HCO^+ wings were checked in the following way. The sum of the widths of the red and blue wings was obtained by subtracting the baseline width of the Gaussian fit of the $H^{13}CO^+$ line from the HCO^+ FWZP. If the sum of the widths was larger than 25 km s^{-1}, then the given source was deemed to have HCO^+ wings. As modelled by Gusdorf et al. (2008; see also Leurini et al. 2014), shocks trigger the erosion of grains, and SiO can be efficiently produced only if shock speeds are above 25 km s^{-1}. Results show (see Table 3) that 28% of our sample (nine sources) present wings in the HCO^+ spectral profile (see e.g. Fig. D.7). However, we note that, due to the lack of spatial information, there is significant uncertainty in these results.

3.2. SiO detection

We checked whether the sources present SiO emission, which directly traces outflows and shocked gas. Emission at 5σ or more was considered. SiO emission was found in 78% of our sample (25 sources). The results are displayed in Table 5.

The material ejected by bipolar outflows forms two lobes, as modelled in Rawlings et al. (2004). Depending on the inclination angle, this produces two main features: the red and blue wings. While centred at the velocity of each source, the width from the Gaussian fit to the $H^{13}CO^+$(2-1) line was subtracted from the SiO(4-3) spectral profile width to obtain the width of the red and blue wings. With these measurements (see Table 5) the velocity integrated intensity of the SiO wings were obtained and further used to calculate the physical properties of the outflows.

There are a few sources that have particularly intense SiO emission, such as source HC02 (associated with IRAS 17574-2403). The peak of the emission of these sources is ≥20 times the RMS and they have $T_{peak} > 0.7$ K. A more detailed description and summary of previous works done on these sources can be found in Appendix C. According to our results, we divided the sample into three groups, as seen in Table 6: 9 sources present both SiO detection and HCO^+ wings, 16 sources present SiO emission and no HCO^+ wings, and the remaining 7 present neither.

Table 5. SiO spectral line data.

Source	R (pc)	RMS (mK)	Full	Red wing	Blue wing	FWZP	Red wing	Blue wing	Position (km s^{-1})	Peak (K)
			Area (K km s^{-1})			Width (km s^{-1})				
HC01	0.26	0.02	0.4	–	–	33.90	–	–	10.1	0.05
HC02	0.26	0.028	26.8	7.5	14.6	92.12	40.11	47.33	10.0	1.11
HC03	0.31	0.02	1.0	0.4	0.5	27.05	13.59	10.64	21.1	0.17
HC04	0.46	0.03	8.4	1.1	3.8	45.55	11.51	26.95	67.2	0.59
HC05	0.25	0.02	2.3	0.5	1.2	43.15	16.95	22.41	33.1	0.22
HC06	0.26	0.02	5.0	2.1	1.7	49.32	24.06	21.35	36.9	0.39
HC07	0.33	0.02	2.5	0.6	1.2	47.26	16.56	27.47	59.4	0.26
HC08	0.38	0.01	13.5	5.5	6.1	74.66	35.58	34.50	−39.1	1.57
HC09	0.47	0.01	1.0	0.4	0.3	36.64	19.13	14.42	−58.1	0.12
HC10	0.40	0.01	0.8	0.1	0.3	19.18	4.88	11.11	−53.5	0.15
HC11	0.31	0.014	0.1	–	–	14.73	–	–	−50.1	0.06
HC12	0.23	0.02	1.3	0.4	0.6	30.82	11.74	17.09	−39.2	0.25
HC13	0.36	0.03	0.0	–	–	0.00	–	–	−67.5	0.08
HC14	0.34	0.03	0.0	–	–	0.00	–	–	−64.7	0.08
HC15	0.44	0.03	2.4	0.6	0.8	29.80	11.34	14.66	−87.9	0.34
HC16	0.33	0.03	6.5	2.4	2.2	42.81	20.25	18.17	−62.9	0.48
HC17	0.425	0.03	12.3	3.3	5.9	56.85	26.33	25.93	−86.7	0.78
HC18	0.28	0.03	15.6	1.3	0.5	36.99	19.59	14.40	−49.4	0.21
HC19	0.27	0.03	0.0	–	–	0.00	–	–	0.0	0.07
HC20	0.29	0.02	11.8	1.3	6.4	50.34	18.90	25.97	−53.3	0.94
HC21	0.28	0.02	2.3	2.9	4.5	60.96	23.95	33.46	−46.3	0.97
HC22	0.23	0.02	19.1	0.8	2.0	87.67	27.45	57.78	−34.6	0.15
HC23	0.24	0.01	1.6	0.6	0.7	44.86	19.48	22.53	−45.8	0.15
HC24	0.24	0.01	1.5	0.6	0.6	46.92	21.63	23.06	−40.3	0.15
HC25	0.40	0.02	0.9	0.3	0.3	31.51	13.29	14.02	−70.3	0.09
HC26	0.24	0.02	1.5	0.4	0.6	30.14	9.84	17.25	−40.5	0.22
HC27	0.25	0.02	17.6	6.1	6.9	74.66	34.50	33.86	−25.3	1.02
HC28	0.34	0.01	0.8	0.3	0.2	31.85	15.56	12.55	−30.8	0.10
HC29	0.48	0.01	2.1	0.8	0.6	42.47	22.89	15.86	−68.5	0.16
HC30	0.24	0.01	0.0	0.9	0.2	45.21	29.28	12.83	18.7	0.15
HC31	0.12	0.013	0.3	–	–	17.81	–	–	−12.5	0.05
HC32	0.325	0.01	0.3	–	–	33.56	–	–	−19.2	0.04

Table 6. Grouping of the sources.

Group	SiO detection	HCO$^+$ wings	No. of sources
A	✓	✓	9
B	✓	–	16
C	–	–	7

4. Results

4.1. Properties of the clump

4.1.1. Virial masses

The Gaussian width of the H^{13}CO$^+$(2-1) spectral line was used to calculate the virial mass of the clump. Assuming that it is gravitationally bound, so that the virial theorem applies, the virial mass can be calculated as (e.g. Merello et al. 2013)

$$\left(\frac{M_{\text{virial}}}{M_\odot}\right) = 210 \left(\frac{\Delta V}{\text{km s}^{-1}}\right)^2 \left(\frac{R}{\text{pc}}\right), \tag{2}$$

where ΔV is the line's Gaussian width and R is the spatial beam size of the source.

The results show (see Table 7) that these sources have very high virial masses, reaching up to $4.9 \times 10^3 M_\odot$. However, the beam of the observation instrument APEX is larger than the clump, and thus the observations include more material.

4.1.2. LTE mass

The local thermodynamic equilibrium (LTE) mass of the clump was calculated using the LTE formalism, assuming the emission is optically thin. The H^{13}CO$^+$ is a linear and rigid rotor molecule. Thus, the column density N_J was calculated as follows (e.g. Garden et al. 1991; Sanhueza et al. 2012):

$$
N_J = \frac{3h}{8\pi^3\mu^2} \frac{U(T_{\text{ex}})}{(J+1)} \frac{\exp\left(\frac{E_J}{kT_{\text{ex}}}\right)}{\left[1 - \exp\left(\frac{-h\nu}{kT_{\text{ex}}}\right)\right]}
$$
$$
\times \frac{1}{\left(J(T_{\text{ex}}) - J(T_{\text{bg}})\right)} \int T_{\text{MB}} d\nu. \tag{3}
$$

Here, k is the Boltzmann constant, h is the Planck constant, $\mu = 3.89 \times 10^{-18}$ (D) is the electric dipole momenta, and

Table 7. Properties obtained from $H^{13}CO^+$ emission.

Source	M_{vir} ($M_\odot$)	N_{tot} (10^{22} cm^{-2})	M_{LTE} ($M_\odot$)	M_{vir}/M_{LTE}	Group
HC01	284	5.36	242	1.17	C
HC02	1181	40.99	1839	0.64	A
HC03	521	8.50	559	0.93	B
HC04	4867	16.39	2381	2.04	B
HC05	760	8.73	376	2.02	B
HC06	828	15.24	693	1.19	A
HC07	735	6.34	485	1.51	B
HC08	1656	14.91	1438	1.15	A
HC09	936	8.37	1245	0.75	B
HC10	849	9.66	1047	0.81	B
HC11	579	2.95	199	2.91	C
HC12	195	4.00	150	1.30	B
HC13	645	9.17	796	0.81	C
HC14	450	3.49	271	1.66	C
HC15	1332	6.81	901	1.48	B
HC16	1334	12.69	937	1.42	A
HC17	1887	8.78	1086	1.74	A
HC18	519	6.16	322	1.61	A
HC19	158	2.35	117	1.35	C
HC20	1829	49.04	2823	0.65	A
HC21	741	178	920	0.81	A
HC22	284	5.92	208	1.37	B
HC23	414	6.14	247	1.68	B
HC24	247	4.07	156	1.58	B
HC25	1488	4.73	526	2.83	B
HC26	465	9.02	352	1.32	B
HC27	2050	16.19	669	3.07	A
HC28	993	5.67	441	2.25	B
HC29	1400	11.12	1772	0.79	B
HC30	473	8.39	318	1.49	B
HC31	227	9.06	83	2.73	C
HC32	360	2.38	172	2.09	C

$E_J = hBJ(J + 1)$ is the energy in the level J (in this case, $J = 1$), where $B = 43377.165$ (MHz) is the rotational constant. The intensity $J(T)$ is defined for a given frequency ν as

$$J(T) = \frac{h\nu}{k} \frac{1}{\exp\left(\frac{h\nu}{kT} - 1\right)}. \tag{4}$$

Finally, $U(T)$ is the partition function

$$U(T) = \sum_{J=0}^{\infty} g_J \exp\left[\frac{-hBJ(J + 1)}{kT_{ex}}\right] \approx \frac{k}{hB}\left(T_{ex} + \frac{hB}{3k}\right), \tag{5}$$

where $g_J = 2J + 1$ is the rotational degeneracy. A cosmic background temperature T_{bg} of 2.75 K was considered. The excitation temperature T_{ex} was set to a standard value of 30 K, which is close to the median of the dust temperatures (26.4 ± 6.0 K; e.g. Elia et al. 2017). The total column density in units of cm^{-2} can be obtained by multiplying N_J by the abundance of $H^{13}CO^+$: $\left[H_2/H^{13}CO^+\right] = 3.0 \times 10^{10}$ (Blake et al. 1987). Finally, the LTE mass was obtained by multiplying the total column density by the area of the source,

$$M_{LTE} = N_{tot}\pi R^2, \tag{6}$$

where R is the radius of the beam. These results are also shown in Table 7.

We compared our LTE mass estimates to the clump mass derived from dust emission obtained by Hi-GAL (Elia et al. 2017, 2021). The ratio of the dust to LTE masses has a mean of 2.11, a median of 1.64, and a standard deviation of 1.34. The origin of this uncertainty can come from the assumed temperature and from the H13CO$^+$ abundance. Furthermore, the dust masses from Hi-GAL used here were calculated by fitting a spectral energy distribuiton (SED) which was scaled to the angular size at 250 μm (Elia et al. 2013; Motte et al. 2010). We note that for the four saturated sources of the sample, the mass used here was obtained using the flux at 500 μm instead (see Appendix A for the treatment of saturated sources). The H^{13}CO$^+$ line and emission at 250 μm trace mostly the same dense gas, and their angular sizes are within a factor of 2.35 on average (see Sect. 3), which is consistent with the difference seen between the masses. This indicates that our estimates are sound.

The uncertainty of the molecular observations is ~20%, which affects the Gaussian fit parameters, and propagates to the rest of the clump's properties. Because of the propagating error, the column density can be considered to have an uncertaintly of 10−20%, whilst the mass uncertainty is <30%. The distances are also a source of uncertainty, which affects the beam radius and masses (see Appendix B).

4.1.3. Virial and LTE mass comparison

The ratio of the virial to LTE mass can provide information about the gravitational stability of the source. High values of this ratio indicate that the internal kinetic energy of the source is too high, and that it is not massive enough to be gravitationally stable. Since the material traced by H^{13}CO$^+$ emission should be both gravitationally bound and in local thermodynamic equilibrium, the virial and LTE mass should match within a factor of ~2 when magnetic effects are not considered. Results are presented in Table 7. The ratio of the virial to LTE mass has a mean value of 1.54, a median of 1.45, a minimum of 0.64, and a maximum of 3.07. Only eight sources have a ratio of 2.00 or higher. Thus, the virial and LTE masses are in good agreement.

4.2. Properties of the SiO outflows

4.2.1. Outflow mass

We calculated the LTE mass for the SiO outflows in the red and blue wings. With an assumption of optically thin thermal SiO(4-3) emission in LTE (e.g. Liu et al. 2021a), the column densities N_J and N_{tot} and the LTE mass were calculated as described in Sect. 4.1.2 using a rotational constant B of 21711.96 (MHz), an electric dipole moment μ of 3.10×10^{-18} (D), an excitation temperature T_{ex} of 18 K, and an SiO abundance [H$_2$/SiO] of 10^9 (Liu et al. 2021a; Sanhueza et al. 2012), standard values for this source type. If a higher T_{ex} of 25 K or 30 K were used, the values of the outflow masses would increase by 16.32 and 29.42%, respectively. Since SiO abundances can drastically vary in different MSF regions (by up to six orders of magnitude; Ziurys et al. 1989; Martin-Pintado et al. 1992; Li et al. 2019b), using an inadequate choice for this parameter could artificially modify the results. Here we use a standard value for [H$_2$/SiO], accepted for protostellar objects. The results are displayed in Table 8.

4.2.2. Dynamical properties

We obtained further characteristics of the outflow (Beuther et al. 2002): momentum P_{out}, kinetic energy E_{kin}, characteristic timescale t, mechanical force or flow of momentum F, rate of matter expulsion $\dot{M}$, and mechanical luminosity or power L_m.

Table 8. Properties of the SiO outflows.

Source	N_R	N_B	M_R	M_B	M_{out}	P_{out}	E_{kin}	t	$\dot{M}$	F	L_m	Group
	(10^{20} cm^{-2})		($M_\odot$)			($M_\odot$ km s^{-1})	(10^{46} erg)	(10^4 yr)	(10^{-4} $M_\odot$ yr^{-1})	(10^{-3} $M_\odot$ km s^{-1} yr^{-1})	($L_\odot$)	
HC02	77.02	150.54	34.5	67.4	101.9	4813	183	0.5	187	884.91	2784	A
HC03	4.34	4.64	2.9	3.0	5.9	79	1	2.2	3	3.54	5	B
HC04	11.78	38.75	17.1	56.2	73.3	1971	17	2.0	37	99.56	69	B
HC05	4.87	11.93	2.1	5.1	7.2	164	3	1.1	6	14.42	19	B
HC06	21.79	17.54	9.9	8.0	17.9	443	12	1.0	17	43.30	97	A
HC07	6.47	12.68	4.9	9.7	14.6	372	5	1.4	11	26.83	29	B
HC08	57.04	63.19	54.9	60.8	115.7	4316	165	1.0	118	438.71	1390	A
HC09	3.83	3.25	5.7	4.8	10.5	194	4	2.5	4	7.81	15	B
HC10	1.36	2.81	1.5	3.0	4.5	48	0.2	4.1	1	1.19	0.4	B
HC12	3.96	6.05	1.5	2.3	3.8	60	1	1.5	3	4.03	3	B
HC15	5.73	7.82	7.6	10.3	17.9	271	3	2.9	6	9.39	9	B
HC16	24.69	22.75	18.2	16.7	34.9	749	17	1.5	23	49.91	97	A
HC17	33.47	60.78	41.3	75.0	116.3	3299	95	1.5	80	225.54	537	A
HC18	13.31	5.63	6.9	2.9	9.9	193	4	1.5	7	13.19	25	A
HC20	13.77	65.74	7.9	37.8	45.7	1255	21	1.1	41	111.37	156	A
HC21	29.53	46.83	15.9	25.2	41.0	1294	27	0.9	46	143.79	249	A
HC22	8.19	20.50	2.9	7.2	10.0	506	8	0.5	20	100.10	135	B
HC23	5.70	7.14	2.3	2.9	5.1	116	2	1.1	5	11.00	18	B
HC24	6.02	6.47	2.3	2.5	4.8	112	2	1.0	5	11.38	21	B
HC25	2.93	3.15	3.3	3.5	6.8	107	2	2.5	3	4.25	5	B
HC26	3.94	5.99	1.5	2.3	3.9	61	0.5	1.5	2	3.95	3	B
HC27	63.10	71.16	26.0	29.3	55.3	2064	78	0.6	86	320.61	1004	A
HC28	2.73	1.71	2.1	1.3	3.4	56	1	2.1	2	2.70	4	B
HC29	8.74	6.45	13.9	10.2	24.1	526	15	2.2	11	23.64	55	B
HC30	9.51	2.36	3.6	0.9	4.5	124	4	1.0	4	12.14	35	B

They were computed as follows:

$$P_{out} = M_r V_r + M_b V_b, \tag{7}$$

$$E_{kin} = \frac{1}{2} M_r V_r^2 + \frac{1}{2} M_b V_b^2, \tag{8}$$

$$t = \frac{2R}{(V_r + V_b)}, \tag{9}$$

$$F_m = \frac{P_{out}}{t}, \tag{10}$$

$$\dot{M}_{out} = \frac{M_{out}}{t}, \tag{11}$$

$$L_m = \frac{E_{kin}}{t}. \tag{12}$$

Here, R is the radius of the source, $M_{out} = M_r + M_b$ is the total outflow mass, and V_b and V_r are the maximum velocities of the outflows, which correspond to $|V_{LSR} - V_i|$ (Beuther et al. 2002; Liu et al. 2021b), where V_i is the velocity at each extreme of the SiO emission baseline. The results are displayed in Table 8.

The uncertainty of the observations (20%; see Sect. 2.2) propagates to these calculated properties. The outflow column density and mass have uncertainties of about 10–20% and <30%, respectively. The momentum and kinetic energy have the same uncertainty as the mass, whilst the force, rate of matter expulsion, and mechanical luminosity have an additional source of uncertainty due to the dynamical timescales, which comes from the distances and the instrumental error (~20%).

A statistical description of these results is shown in Table 9. The typical rate of matter expulsion for mid and early massive protostars ranges from 10^{-5} to a few times $10^{-3} M_\odot$ yr^{-1}, and the typical momentum from 10^{-4} to 10^{-2} $M_\odot$ km s^{-1} (Arce et al. 2007). Our results for the rate of matter expulsion are well within this typical range. The momentum is generally higher, with a mean of 922 $M_\odot$ km s^{-1}, indicating that the outflows in our sample are generally very fast and/or massive. Furthermore, the SiO outflows studied here present properties that are within the range of results presented in other works, but are more massive and powerful. This is the case for the sample of protostellar candidates studied by Beuther et al. (2002), which were traced with CO(2-1), and the sample of massive young stellar objects (MYSOs) and compact HII regions traced with ^{12}CO(2-1) and ^{13}CO(2-1) by Maud et al. (2015). Similarly, our sample has more massive and powerful SiO outflows than other studies that have traced them with the SiO(5-4) spectral line, such as the sample of infrared dark clouds (IRDCs) studied by Liu et al. (2021a), for which our results are larger by up to three orders of magnitude. Thus, our results are in good agreement with other works in the literature, and our sources stand out because of their powerful outflows.
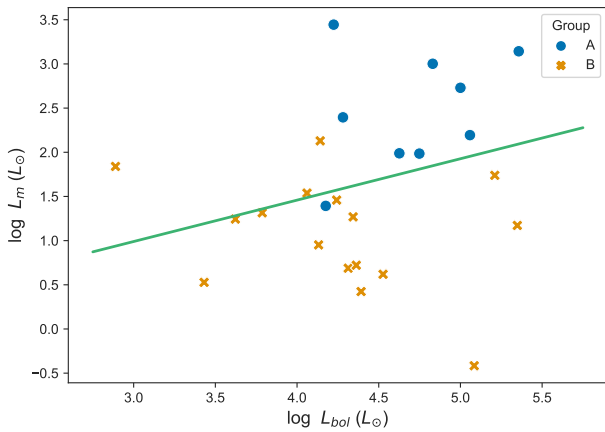
5. Discussion

5.1. Correlations

We looked for correlations between the properties of the outflows and the properties of their hosting clump. We found three relevant correlations: between the bolometric luminosity and outflow power, between the outflow power and the rate of matter

**Table 9.** Statistics of the properties of the outflow.

	M_{out} ($M_\odot$)	P_{out} ($M_\odot$ km s^{-1})	E_{kin} (10^{46} erg)	t (10^4 yr)	$\dot{M}$ ($10^{-4} M_\odot$ yr^{-1})	F ($10^{-3} M_\odot$ km s^{-1} yr^{-1})	L_m ($L_\odot$)
Mean	30	928	27	1.6	29	102.69	271
STD.	36	1358	50	0.8	45	196.34	622
Min.	3	48	0.2	0.5	1	1.19	0.4
25%	5	112	2	1.0	4	7.81	9
Median	11	271	4	1.5	7	14.42	29
75%	41	1255	17	2.1	37	100.10	135
Max.	116	4813	183	4.1	187	884.91	2784

Fig. 4. Bolometric luminosity ($L_\odot$) vs. outflow power L_m ($L_\odot$) in logarithmic scale.

Fig. 5. Kinetic energy (10^{46} erg) vs. outflow mass ($M_\odot$) in logarithmic scale. The Spearman ρ rank correlation coefficient is equal to 0.93 and the slope is equal to 0.69.

expulsion, and between the kinetic energy of the outflow and outflow mass. Their rank correlation coefficients were calculated, and the Python package `sklearn.linear_model` (Pedregosa et al. 2011) was used to perform a linear regression in order to find the slope of these correlations. Our results show that, for these three correlations, the rank correlation coefficients are positive, as are the slopes.

A weak linear trend between the bolometric luminosity and the outflow power shown in Fig. 4 was found. This correlation tells us that, given a source with a molecular outflow, the more luminous the source, the more energetic its outflow will be. Therefore, it is possible that it will power more massive and energetic outflows. However, this correlation has a large amount of dispersion, and it is not possible to make definitive conclusions. Other studies have also found this correlation: Wu et al. (2004), Liu et al. (2021b), and Maud et al. (2015) found it in the ^{12}CO and ^{13}CO lines, and Liu et al. (2021b) also found it in the HCO$^+$ and CS lines. It has also been found in other SiO transitions (Csengeri et al. 2016; Li et al. 2019b; Liu et al. 2021a). All of these species are outflow tracers and the linear regressions have always given a positive slope. Thus, although it is a weak correlation in our sample, it is still positive and is in agreement with the trends found by these other works. Thus, the idea that more luminous sources are able to produce more powerful shocks (Codella et al. 1999) cannot be discarded. Since this has been found in various SiO transitions and outflow tracers, and now in SiO(4-3) as well, it is a possible universal trend to molecular outflows in MSF regions.

As shown in Fig. 5, there is a close linear relationship between the kinetic energy and the outflow mass. This
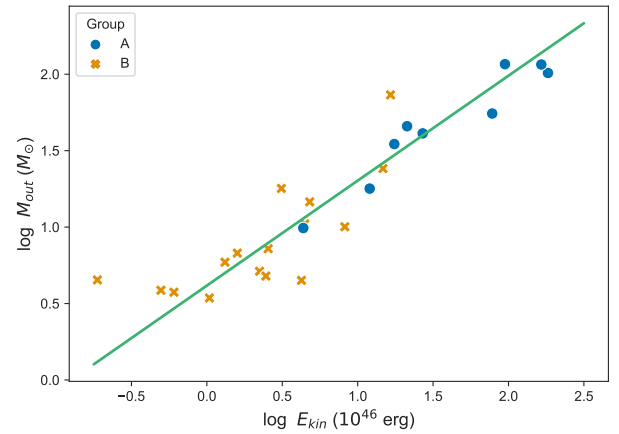
correlation has a Spearman ρ coefficient of 0.93 and a slope of 0.69. It is strong, and suggests that the more massive an outflow is, the faster it will be.

It should be noted that this correlation is physically equivalent to that between the outflow power and the rate of mass expulsion, as these parameters are proportional to the inverse of the characteristic timescale (see Eqs. (11) and (12)):

$$ t = \frac{M_{out}}{\dot{M}_{out}} = \frac{E_{kin}}{L_m}. \tag{13} $$

Thus, this correlation carries the uncertainties of the dynamical timescale previously discussed. However, it is still useful to analyse this trend as it provides intuitive physical significance, and a direct comparison with other works is possible. In our sample this is a strong relation; its Spearman ρ rank correlation coefficient is equal to 0.97 and its slope is equal to 0.70 (see Fig. 6). This relationship tells us that the more powerful the outflow is, the faster it ejects matter. Therefore, in addition to expelling more material, energetic outflows expel this material faster. This trend has also been found by other studies, such as Beuther et al. (2002) and Liu et al. (2021b) in the CO line and its isotopologues. Liu et al. (2021b) found this trend in other outflow tracers as well, such as HCO$^+$ and CS, indicating that this trend is common to outflows independent of the tracer used. Finding this trend in SiO here further supports this idea.

The correlations found here suggest that since sources with a larger bolometric luminosity are more energetic, their outflows are as well. These energetic outflows are able to mobilise
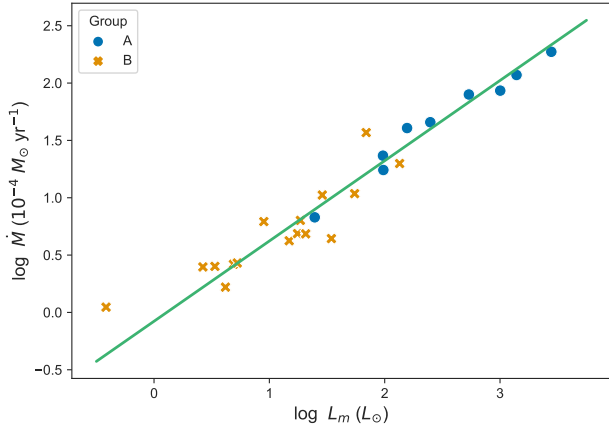
Fig. 6. Outflow power L_m ($L_\odot$) vs. rate of matter expulsion $\dot{M}$ ($10^{-4} M_\odot$ yr^{-1}) in logarithmic scale. The Spearman ρ rank correlation coefficient is equal to 0.97 and the slope is equal to 0.70.

more material. Thus, their rate of mass loss is high, which translates into high outflow masses. These correlations agree with the dependency suggested by Liu et al. (2021b; see also Wu et al. 2004): bolometric luminosity → outflow energy → rate of mass loss → outflow mass.

5.2. Evolutionary stage indicator L/M

The luminosity-to-mass ratio L/M can be used as an evolutionary stage indicator (e.g. Molinari et al. 2016; Elia et al. 2021; Urquhart et al. 2022). In the first stages of star formation the core is cold and actively accreting matter, so $L/M \leq 1$. Eventually, the temperature and luminosity increase, while the mass remains virtually unchanged. This results in a value of $L/M \geq 1$. It has been found that the more luminous sources in the Galaxy usually have $L/M \geq 10$ (López-Sepulcre et al. 2011; Molinari et al. 2016). The sources in the sample studied here are in an advanced stage of the star-forming process as L/M has values ranging from 3 $L_\odot/M_\odot$ up to 177 $L_\odot/M_\odot$, with a mean of 58 $L_\odot/M_\odot$ and a median of 41 $L_\odot/M_\odot$ (see Table 2). Furthermore, we looked for correlations between L/M and the SiO outflow properties and found that they are not correlated. Other works have also failed to find such correlations (Liu et al. 2022, 2021b; Maud et al. 2015). This strongly suggests that molecular outflows are present throughout the whole of the high-mass star formation process (Csengeri et al. 2016; Urquhart et al. 2022).

5.3. Cross-check between SiO and HCO+ wing detections

All of the sources that present wings in the HCO+ line also present SiO emission above 5σ. We compared these sources (Group A) with the rest of the clumps with SiO detections (Group B; see Table 6). Table 10 shows a statistical comparison of the spectral parameters, the outflow properties, and the evolutionary stage indicator L/M between these groups.

SiO spectral profiles with FWZP > 20 km s^{-1} are considered broad line widths due to high-velocity shocks (Duarte-Cabral et al. 2014; Zhu et al. 2020). We note that all the sources in both Groups A and B exhibit broad line widths, with a minimum FWZP of 19.18 km s^{-1}, a mean value of 47.15 km s^{-1}, a median value of 44.86 km s^{-1}, and a maximum of 92.12 km s^{-1}. This means that all of the sources where SiO was detected have experienced recent outflow activity, which has manifested in high-velocity shocks, typically associated with collimated jets,

and it is strong enough to produce SiO outflows (Csengeri et al. 2016; Li et al. 2019b; Liu et al. 2022). This confirms the sources in both Groups A and B are protostellar (Zhu et al. 2020).

Furthermore, the SiO spectral profile of the sources in Group A is wider and more intense, indicating that the outflows in this group are more massive, faster and more energetic than those in Group B (Schilke et al. 1997; Duarte-Cabral et al. 2014; Liu et al. 2022; see Table 10). Their mean outflow mass is higher than those in Group B by a factor of 4.8, their mean momentum by a factor of 7, their mean kinetic energy by a factor of 14.7, their dynamic timescale by a factor of 0.58, their rate of matter expulsion by a factor of 8.7, their outflow force by a factor of 12, and their outflow power by a factor of 25.1. Sources in Group A are possibly more collimated too, as broad-width SiO detection is associated with them. Further studies of the spatial morphology of these outflows could confirm this trend.

Even though SiO outflow activity has been found to decrease and become less collimated over time (Arce et al. 2007; Sakai et al. 2010; López-Sepulcre et al. 2011), results show that sources in Groups A and B are virtually at the same stage of evolution because their evolutionary stage indicator L/M have similar values. Table 10 shows that the evolutionary stage indicator L/M has a mean value of 40 ($L_\odot/M_\odot$) and 47 ($L_\odot/M_\odot$), and a median of 32 ($L_\odot/M_\odot$) and 29 ($L_\odot/M_\odot$) for Groups A and B, respectively. Thus, sources in Groups A and B are most likely equally evolved, even within the protostellar phase (Motte et al. 2018). The fact that sources in Group A have more intense and massive SiO outflows, but both groups are at the same evolutionary stage, suggests that the presence of wings in the HCO+ spectral profile could help identify sources with stronger SiO outflows. Therefore, checking for wings in the HCO+ line could help identify more massive and active MSF regions in samples of similarly evolved sources. Alternatively, since HCO+ emission is associated with old outflow activity (Li et al. 2019a), sources in Group B might have just recently started exhibiting strong outflow activity, thus allowing SiO outflows to be detected, and are too new to produce wings in the HCO+ spectral profile. Meanwhile, sources in Group A might have started exhibiting outflow activity long enough ago for wings in the HCO+ spectral profile, a signal of old outflows, to form. In this scenario, SiO outflows detected from the sources in Group A have been active for a longer time, which might be a consequence of their high mass, power, and luminosity. Thus, checking for wings in the HCO+ line might also help identify sources whose outflows have been active for longer. Further research with larger samples and better resolution could provide insight into which of these two scenarios is more likely and significant.

6. Summary and conclusions

The aim of this work was to study shocked matter and SiO outflows in very massive, luminous, and powerful protostellar sources. We characterised them, searched for any evolutionary trends they might exhibit, associated the presence of shocked gas with outflow activity, and cross-checked SiO emission with other outflow signatures. We used single-dish APEX/SEPIA Band 5 observations of 32 of the brightest massive protostellar sources in the southern Galaxy. We studied their outflow activity using the SiO and HCO+ tracers, as well as their general clump properties with H^{13}CO+ emission. The following is a summary of our main results and conclusions:

1. The SiO emission detection rate above 5σ is 78% (25 sources). All SiO detections have a broad line width due

Table 10. Statistics of the spectral parameters and outflow properties of sources from Groups A and B.

	FWZP (km s^{-1})		Peak (K)		Full area (K km s^{-1})		$M_{\rm out}$ ($M_\odot$)		$P_{\rm out}$ ($M_\odot$ km s^{-1})		$E_{\rm kin}$ (10^{46} erg)		t (10^4 yr)		$\dot{M}$ ($10^{-4} M_\odot$ yr^{-1})		F ($10^{-3} M_\odot$ km s^{-1} yr^{-1})		L_m ($L_\odot$)		L/M ($L_\odot/M_\odot$)	
Group	A	B	A	B	A	B	A	B	A	B	A	B	A	B	A	B	A	B	A	B	A	B
Mean	59.86	40.01	0.8	0.2	12.4	3.0	60	13	2047	298	67	4	1.1	1.9	67	8	247.93	21.00	704	27	40	47
STD	17.69	15.29	0.4	0.1	7.4	4.7	41	17	1705	472	68	5	0.4	0.9	58	9	276.95	31.61	910	35	33	45
Min.	36.99	19.18	0.2	0.1	2.3	0.04	10	3	193	48	4	0.2	0.5	0.5	7	1	13.19	1.19	25	0.4	3	3
25%	49.32	30.65	0.5	0.2	6.5	1.0	35	5	749	75	17	1	0.9	1.1	23	3	49.91	4.01	97	5	12	17
Median	56.85	39.56	0.9	0.2	12.3	1.5	46	6	1294	120	27	3	1.0	1.8	46	5	143.79	10.20	249	17	32	29
75%	74.66	45.30	1.0	0.2	15.6	2.3	102	12	3299	296	95	4	1.5	2.3	86	7	320.61	16.73	1004	31	71	52
Max.	92.12	87.67	1.6	0.6	26.8	19.1	116	73	4813	1971	183	17	1.5	4.1	187	37	884.91	100.10	2784	135	81	151

to high-velocity shocks, which confirms that these sources have evolved well into the protostellar phase. Furthermore, 28% of our sample (nine sources) show wings in the HCO$^+$ spectral profile.

2. We calculated the dynamical properties of the SiO outflows. Results show they are very massive, fast, and energetic. The outflow mass has a minimum value of 3 $M_\odot$, a median of 10 $M_\odot$, a mean of 30 $M_\odot$, and a maximum value of 116 $M_\odot$. The outflow momentum has a minimum value of 50 $M_\odot$ km s^{-1}, a median of 271 $M_\odot$ km s^{-1}, a mean of 922 $M_\odot$ km s^{-1}, and a maximum value of 4812 $M_\odot$ km s^{-1}. The kinetic energy of the outflow has a minimum value of 0.1×10^{46} erg, a median of 4×10^{46} erg, a mean of 27×10^{46} erg, and a maximum value of 183×10^{46} erg. The outflow power has a minimum value of $1.24 \times 10^{-3} M_\odot$ km s^{-1} yr^{-1}, a median of $14.24 \times 10^{-3} M_\odot$ km s^{-1} yr^{-1}, a mean of $102.25 \times 10^{-3} M_\odot$ km s^{-1} yr^{-1}, and a maximum value of $884.85 \times 10^{-3} M_\odot$ km s^{-1} yr^{-1}.

3. We found three positive linear correlations involving SiO outflows properties: a weak one between the bolometric luminosity and outflow power (Fig. 4), a strong one between the outflow power and the rate of matter expulsion (Fig. 6), and another strong one between the kinetic energy and outflow mass (Fig. 5). They are all positive correlations. The second and third have very low dispersion, but the second has high dispersion. These correlations suggest that the more energetic the outflow, the more material it is able to mobilise.

4. We did not find any correlations between the evolutionary stage indicator L/M and SiO outflow properties. This agrees with the idea that molecular outflows are a ubiquitous phenomenon throughout the process of high-mass star formation.

5. We performed a cross-check between SiO detection and the presence of wings in the HCO$^+$ line. Sources in Group A (sources that present both features; see Table 6) have more massive, faster, more energetic, and more collimated SiO outflows than sources in Group B (sources that only exhibit SiO emission). The sources in both groups are at an advanced stage of evolution in the high-mass star formation process, and there is no clear evolutionary difference between them. Thus, since SiO emission is such a good tracer of outflow activity, checking for wings in the HCO$^+$ line could help identify more massive and active MSF regions in samples of similarly evolved sources. Alternatively, checking for wings in the HCO$^+$ line might help identify sources whose outflows have been active for longer, since HCO$^+$ traces old outflow activity, whilst SiO traces recent and active outflows.

Our findings show the potential for further studies of sources at an advanced stage of evolution ($L/M > 10$) and their molecular outflows.

References

Acord, J. M., Walmsley, C. M., & Churchwell, E. 1997, ApJ, 475, 693
Araya, E., Hofner, P., Kurtz, S., Bronfman, L., & DeDeo, S. 2005, ApJS, 157, 279
Arce, H. G., Shepherd, D., Gueth, F., et al. 2007, in Protostars and Planets V, eds. B. Reipurth, D. Jewitt, & K. Keil (Tucson: University of Arizona Press), 245
Bally, J. 2016, ARA&A, 54, 491
Baug, T., Wang, K., Liu, T., et al. 2020, ApJ, 890, 44
Belitsky, V., Lapkin, I., Fredrixon, M., et al. 2018, A&A, 612, A23
Beuther, H., Schilke, P., Menten, K. M., et al. 2002, ASP Conf. Ser., 267, 341
Blake, G. A., Sutton, E. C., Masson, C. R., & Phillips, T. G. 1987, ApJ, 315, 621
Bronfman, L., Nyman, L. A., & May, J. 1996, A&AS, 115, 81
Butler, M. J., & Tan, J. C. 2012, ApJ, 754, 5
Codella, C., Bachiller, R., & Reipurth, B. 1999, A&A, 343, 585
Csengeri, T., Leurini, S., Wyrowski, F., et al. 2016, A&A, 586, A149
De Buizer, J. M., Redman, R. O., Longmore, S. N., Caswell, J., & Feldman, P. A. 2009, A&A, 493, 127
Dedes, C., Leurini, S., Wyrowski, F., et al. 2011, A&A, 526, A59
De Simone, M., Codella, C., Ceccarelli, C., et al. 2022, MNRAS, 512, 5214
Duarte-Cabral, A., Bontemps, S., Motte, F., et al. 2014, A&A, 570, A1
Duronea, N. U., Cichowolski, S., Bronfman, L., et al. 2021, A&A, 646, A103
Dutrey, A., Guilloteau, S., & Guelin, M. 1997, A&A, 317, L55
Elia, D., Molinari, S., Fukui, Y., et al. 2013, ApJ, 772, 45
Elia, D., Molinari, S., Schisano, E., et al. 2017, MNRAS, 471, 100
Elia, D., Merello, M., Molinari, S., et al. 2021, MNRAS, 504, 2742
Fernández-López, M., Sanhueza, P., Zapata, L. A., et al. 2021, ApJ, 913, 29
Figuerêdo, E., Blum, R. D., Damineli, A., & Conti, P. S. 2005, AJ, 129, 1523
Garay, G., Brooks, K. J., Mardones, D., Norris, R. P., & Burton, M. G. 2002, ApJ, 579, 678
Garay, G., Mardones, D., Bronfman, L., et al. 2010, ApJ, 710, 567
Garden, R. P., Hayashi, M., Gatley, I., Hasegawa, T., & Kaifu, N. 1991, ApJ, 374, 540
Gómez, L., Wyrowski, F., Schuller, F., Menten, K. M., & Ballesteros-Paredes, J. 2014, A&A, 561, A148
Gusdorf, A., Cabrit, S., Flower, D. R., & Pineau des Forêts, G. 2008, A&A, 482, 809
He, Y.-X., Henkel, C., Zhou, J.-J., et al. 2021, ApJS, 253, 2
Henning, T., Lapinov, A., Schreyer, K., Stecklum, B., & Zinchenko, I. 2000, A&A, 364, 613
Jiao, W., Wang, K., Pillai, T. G. S., et al. 2023, ApJ, 945, 81
Klaassen, P. D., & Wilson, C. D. 2007, ApJ, 663, 1092

Krishnan, V., Ellingsen, S. P., Voronkov, M. A., & Breen, S. L. 2013, MNRAS, 433, 3346

Lee, J.-K., Walsh, A., Burton, M., & Ashley, M. 2001, MNRAS, 324, 1102

Lee, J. K., Walsh, A. J., & Burton, M. G. 2002, IAU Symp., 206, 175

Leurini, S., Codella, C., López-Sepulcre, A., et al. 2014, A&A, 570, A49

Leurini, S., Wyrowski, F., Wiesemeyer, H., et al. 2015, A&A, 584, A70

Li, Q., Zhou, J., Esimbek, J., et al. 2019a, MNRAS, 488, 4638

Li, S., Wang, J., Fang, M., et al. 2019b, ApJ, 878, 29

Li, S., Zhang, Q., Pillai, T., et al. 2019c, ApJ, 886, 130

Li, S., Sanhueza, P., Zhang, Q., et al. 2020, ApJ, 903, 119

Liu, H.-L., Sanhueza, P., Liu, T., et al. 2020, ApJ, 901, 31

Liu, M., Tan, J. C., Marvil, J., et al. 2021a, ApJ, 921, 96

Liu, D.J., D.-J., Xu, Y., Li, Y.-J., et al. 2021b, ApJS, 253, 15

Liu, R., Liu, T., Chen, G., et al. 2022, MNRAS, 511, 3618

Lo, N., Cunningham, M., Bains, I., Burton, M. G., & Garay, G. 2007, MNRAS, 381, L30

Lo, N., Cunningham, M. R., Jones, P. A., et al. 2014, ApJ, 797, L17

López-Sepulcre, A., Walmsley, C. M., Cesaroni, R., et al. 2011, A&A, 526, L2

López-Sepulcre, A., Watanabe, Y., Sakai, N., et al. 2016, ApJ, 822, 85

Martin-Pintado, J., Bachiller, R., & Fuente, A. 1992, A&A, 254, 315

Maud, L. T., Moore, T. J. T., Lumsden, S. L., et al. 2015, MNRAS, 453, 645

Merello, M., Bronfman, L., Garay, G., et al. 2013, ApJ, 774, 38

Merello, M., Molinari, S., Rygl, K. L. J., et al. 2018, MNRAS, 483, 5355

Mladenović, M. 2017, AIP, 147, 24

Molinari, S., Merello, M., Elia, D., et al. 2016, ApJ, 826, L8

Morales, E. F. E., Mardones, D., Garay, G., Brooks, K. J., & Pineda, J. E. 2009, ApJ, 698, 488

Motte, F., Bontemps, S., Schilke, P., et al. 2007, A&A, 476, 1243

Motte, F., Zavagno, A., Bontemps, S., et al. 2010, A&A, 518, L77

Motte, F., Bontemps, S., & Louvet, F. 2018, ARA&A, 56, 41

Murphy, T., Cohen, M., Ekers, R. D., et al. 2010, MNRAS, 405, 1560

Myers, P. C., Mardones, D., Tafalla, M., Williams, J. P., & Wilner, D. J. 1996, ApJ, 465, L133

Nicholas, B., Rowell, G., Burton, M. G., et al. 2011a, MNRAS, 411, 1367

Nicholas, B. P., Rowell, G., Burton, M. G., et al. 2011b, MNRAS, 419, 251

Olguin, F. A., Sanhueza, P., Guzmán, A. E., et al. 2021, ApJ, 909, 199

Ossenkopf, V., & Henning, T. 1994, A&A, 291, 943

Pedregosa, F., Varoquaux, G., Gramfort, A., et al. 2011 J. Mach. Learn. Res., 12, 2825

Rawlings, J. M. C., Redman, M. P., Keto, E., & Williams, D. A. 2004, MNRAS, 351, 1054

Reid, M. J., Menten, K. M., Zheng, X. W., et al. 2009, ApJ, 700, 137

Reid, M. J., Menten, K. M., Brunthaler, A., et al. 2014, ApJ, 783, 130

Reid, M. J., Menten, K. M., Brunthaler, A., et al. 2019, ApJ, 885, 131

Rojas-García, O. S., Gómez-Ruiz, A. I., Palau, A., et al. 2022, ApJS, 262, 13

Sakai, T., Sakai, N., Hirota, T., & Yamamoto, S. 2010, ApJ, 714, 1658

Sanhueza, P., Jackson, J. M., Foster, J. B., et al. 2012, ApJ, 756, 60

Schilke, P., Walmsley, C. M., Pineau des Forets, G., & Flower, D. R. 1997, A&A, 321, 293

Shirley, Y. L. 2015, PASP, 127, 299

Sollins, P. K., Hunter, T. R., Battat, J., et al. 2004, ApJ, 616, L35

Su, Y.-N., Liu, S.-Y., Wang, K.-S., Chen, Y.-H., & Chen, H.-R. 2009, ApJ, 704, L5

Tang, Y.-W., Ho, P. T. P., Girart, J. M., et al. 2009, ApJ, 695, 1399

Testi, L., Felli, M., Persi, P., & Roth, M. 1998, A&AS, 129, 495

Urquhart, J. S., Wells, M. R. A., Pillai, T., et al. 2022, MNRAS, 510, 3389

van der Tak, F. F. S. 2004, in Star Formation at High Angular Resolution, eds. M. G. Burton, R. Jayawardhana, & T. L. Bourke (Amsterdam: Elsevier), 221, 59

van der Tak, F. F. S., Shipman, R. F., Jacq, T., et al. 2019, A&A, 625, A103

Voronkov, M. A., Caswell, J. L., Ellingsen, S. P., Green, J. A., & Breen, S. L. 2014, MNRAS, 439, 2584

Widmann, F., Beuther, H., Schilke, P., & Stanke, T. 2016, A&A, 589, A29

Wiles, B., Lo, N., Redman, M. P., et al. 2016, MNRAS, 458, 3429

Wu, Y., Wei, Y., Zhao, M., et al. 2004, A&A, 426, 503

Wu, Y., Zhu, M., Wei, Y., et al. 2005, ApJ, 628, L57

Yang, A. Y., Urquhart, J. S., Wyrowski, F., et al. 2022, A&A, 658, A160

Yu, N., & Wang, J.-J. 2015, MNRAS, 451, 2507

Yu, N.-P., Xu, J.-L., & Wang, J.-J. 2018, RAA, 18, 015

Zahorecz, S., Jimenez-Serra, I., Testi, L., et al. 2017, A&A, 602, L3

Zapata, L. A., Ho, P. T. P., Guzmán Ccolque, E., et al. 2019, MNRAS, 486, L15

Zapata, L. A., Ho, P. T. P., Fernández-López, M., et al. 2020, ApJ, 902, L47

Zhu, F.-Y., Wang, J.-Z., Liu, T., et al. 2020, MNRAS, 499, 6018

Zinchenko, I., Henkel, C., & Mao, R. Q. 2000, A&A, 361, 1079

Ziurys, L. M., Friberg, P., & Irvine, W. M. 1989, ApJ, 343, 201

Appendix A: Treatment of saturated sources

There are four sources in our sample with saturated observations (flagged with a ♦ in Tables 1 and 2): HC02, HC04, HC16, and HC20. Their dust mass M_d was estimated at 500 μm (e.g. Merello et al. 2013; Motte et al. 2007),

$$M_d = \frac{F_\nu D^2}{\kappa_\nu B_\nu(T_d)}, \qquad (A.1)$$

where D is the distance to the source, F_ν is the flux density obtained from the Hi-GAL catalogue Elia et al. (2021), κ_ν is the opacity, and $B_\nu(T_d)$ is Planck's function at frequency $\nu =$ 599.585 GHz. The dust temperature T_d was set to 25 K. The opacity κ_{500} for dense clumps with typical conditions has a value of 5.04 cm^2 g^{-1} at 500 μm (Ossenkopf & Henning 1994).

The bolometric luminosity L_{bol} was calculated using the flux density at 70 μm obtained from the Hi-GAL catalogue, which has been found to be a good estimator for the total luminosity of protostellar objects when using the following empirical relation (Elia et al. 2017):

$$L_{bol}(L_\odot) = 2.56 \cdot F_{70}{}^{1.00}(Jy) \qquad (A.2)$$

Appendix B: Distances

The distances used for the selection of the sources D_{sel} are the kinematic distances from Reid et al. (2009) using the local standard of rest velocity V_{LSR} taken from Bronfman et al. (1996). Once the selection was made, the distances to the sources were corrected, as seen in Table B.1. The distance measured through trigonometric parallax from Reid et al. (2019) was used for the sources that have it. For the sources that do not have a distance calculated with parallax, the kinematic distances from Reid et al. (2014) were used instead. This left us with distances with the least possible uncertainty. These corrected distances were the ones used in the calculation of the properties of the sources.

Source	D_{sel} (kpc)	D_{new} (kpc)	Type
HC01	2.33	2.95	Parallax
HC02	2.25	2.94	Parallax
HC03	3.64	3.56	Parallax
HC04	5.49	5.29	Parallax
HC05	3.42	2.88	Parallax
HC06	3.61	2.96	Parallax
HC07	4.27	3.84	Parallax
HC08	4.31	4.31	Kinematic
HC09	5.35	5.35	Kinematic
HC10	4.30	4.57	Kinematic
HC11	3.37	3.60	Kinematic
HC12	2.53	2.69	Kinematic
HC13	4.04	4.09	Kinematic
HC14	3.81	3.87	Kinematic
HC15	5.08	5.05	Kinematic
HC16	3.68	3.77	Kinematic
HC17	4.90	4.88	Kinematic
HC18	3.05	3.17	Kinematic
HC19	3.00	3.10	Kinematic
HC20	3.22	3.33	Kinematic
HC21	3.13	3.22	Kinematic
HC22	2.60	2.60	Parallax
HC23	3.37	2.78	Parallax
HC24	3.17	2.72	Parallax
HC25	3.26	4.63	Kinematic
HC26	3.37	2.74	Parallax
HC27	2.29	2.82	Kinematic
HC28	3.78	3.87	Kinematic
HC29	5.61	5.54	Kinematic
HC30	2.78	2.70	Parallax
HC31	2.16	1.33	Parallax
HC32	4.15	3.73	Parallax

Table B.1. Distances to the sources in the studied sample.

Appendix C: Notes on particular sources

Some of the sources in our sample were found to be of particular interest because the intensity of their SiO outflows stands out from the rest (peak > 0.7 K). They are all of potential interest for future work. A brief description of the studies that have been carried out on these sources is provided here.

C.1. HC02: HIGALBM5.8856-0.3920, IRAS 17574-2403

This source (see Fig. 3) presents a particularly intense outflow. Although it is not the most massive, it has the maximum rate of matter expulsion calculated here. In addition, its spectral profiles shown in Fig. 3 suggest that there is a second cloud at 15.7 km s^{-1}, and absorption at $\sim$ 20 km s^{-1}. It has been extensively studied since its discovery (Acord et al. 1997). Zahorecz et al. (2017) observed this source with APEX in the Band 5 and found that it does not present D_2CO emission, suggesting that it is past the early stages of evolution. It was mapped at 12 mm and 7 mm by Nicholas et al. (2011a) and Nicholas et al. (2011b), respectively, and its [OI] spectra were resolved by Leurini et al. (2015). Its magnetic fields were studied by Tang et al. (2009) and Fernández-López et al. (2021). Su et al. (2009) reported a dense and hot-molecular cocoon in the environment of the source. Furthermore, its outflow has been extensively studied. The outflow of this source was mapped in the SiO(5-4) line by Sollins et al. (2004), traced in the SiO(8-7) line by Klaassen & Wilson (2007), and Zapata et al. (2019) found indications that it is an explosive multi-polar outflow. This was confirmed in Zapata et al. (2020), where a graph and an animation modelling the source are presented, clearly showing the multiple lobes.

C.2. HC08: HIGALBM301.1365-0.2259, IRAS 12326-6245

This source (see Fig. D.7) presents the most intense (T_{peak} = 1.57 K) SiO emission in our sample and the most massive outflow (M_{out} = 116$M_\odot$). There are multiple infrared and radio sources deeply embedded in this clump (Henning et al. 2000; Murphy et al. 2010), and it presents one of the strongest molecular outflows in the southern sky (Araya et al. 2005). This suggests it is already at an advanced stage of evolution (Dedes et al. 2011). Finally, Duronea et al. (2021) present a study of the IR bubble S169 associated with this source, and conclude that star formation is actively taking place.

C.3. HC17: HIGALBM331.2786-0.1883, IRAS 16076-5134

This source presents one of the strongest outflows in our sample, which is clearly seen in both its HCO$^+$ and SiO lines (see Fig. D.16). Its HCO$^+$ line presents significant absorption and the SiO profile is one of the widest in our sample (FWZP = 52.26 km s^{-1}). It has been an object of interest in numerous studies. Zinchenko et al. (2000) present C^{18}O and HNCO observations and find that HNCO emission is most likely related to shocks of matter, similar to SiO emission. They detected HNCO emission in this source. Lee et al. (2001) and Lee et al. (2002) reported shock-excited H$_2$ emission in addition to an outflow powered by a deeply embedded object in the former. Furthermore, De Buizer et al. (2009) present single-dish SiO(6–5) observations and evidence of outflow, and Baug et al. (2020) present images of the CO outflow observed with ALMA.

C.4. HC20: HIGALBM333.1246-0.4244, IRAS 16172-5028

The SiO intensity and the clear asymmetry of the spectral lines of this source make it particularly interesting. As is clear in Fig. D.19, its HCO$^+$ line experiences more absorption on the blue side than on the red side. The H^{13}CO$^+$ even shows a wing on the red side, indicating that the outflow is particularly intense. The SiO line has a particular profile: its intensity decreases at the same velocity as the HCO$^+$ absorption and the H^{13}CO$^+$ wing. This suggests that there might be a second colder cloud at around 50 km s^{-1}. Rojas-García et al. (2022) map this source at 216.968 GHz and also report the possibility of a second source nearby. They also present a chemical profile of this source, where several COMs and SiO are detected. This source was also studied by Lo et al. (2007), where strong SiO and water maser emissions were detected. Lo et al. (2014) present a [CI] mapping of the source. Moreover, Figuerêdo et al. (2005) show that this source contains an embedded OB star cluster at very early evolutionary stages, and the presence of infall was confirmed by Wiles et al. (2016).

C.5. HC21: HIGALBM335.5848-0.2894, IRAS 16272-4837

This source presents one of the most intense (97.0 km s^{-1}) and wide (57.41 km s^{-1}) SiO profiles in the sample, as clearly seen in Fig. D.20. The studies done on this source include the discovery of water emission towards this source (van der Tak, F. F. S. et al. 2019), which has also been used as an evolutionary indicator because it can only be detected when the inner hot gas has reached a temperature of at least 300 K (van der Tak 2004). Emission of HNCO, another shock tracer, was found by Yu et al. (2018). Moreover, Garay et al. (2002) suggest that there is a young massive protostar embedded in this clump and it is still undergoing an intense accretion phase. This corresponds well with our findings and further suggests that it is a HMC. Finally, ALMA observations of this source have been presented by Olguin et al. (2021), where there is evidence of infall and rotation motions.

C.6. HC27: HIGALBM345.0035-0.2239, IRAS 17016-4124

This source presents a very wide (68.36 km s^{-1}) and intense (1.02 K) SiO emission (see Fig. D.26). In addition, its HCO$^+$ profile presents significant self-absorption and absorption. These characteristics make it a particularly interesting source. Several studies have conducted observations towards this source. Zinchenko et al. (2000) present C^{18}O and HNCO emission observations, where it was found that high-velocity gas enhances the abundance of HNCO. Furthermore, mid-infrared observations are presented by Morales et al. (2009), and Testi et al. (1998) present H$_2$O maser emission detection. Krishnan et al. (2013) and Voronkov et al. (2014) have found methanol maser emission as well. This source has been mapped with Large APEX BOlometer CAmera (LABOCA) at APEX by Gómez et al. (2014). Finally, Yu & Wang (2015) present MALT90 (Millimetre Astronomy Legacy Team 90 GHz) observations of the N$_2$H$^+$, H^{13}CO$^+$, HCO$^+$, HNC, C$_2$H, HC$_3$N, and SiO spectral lines, and conclude that the sources in their sample are associated with dense clumps and recent outflow activity.
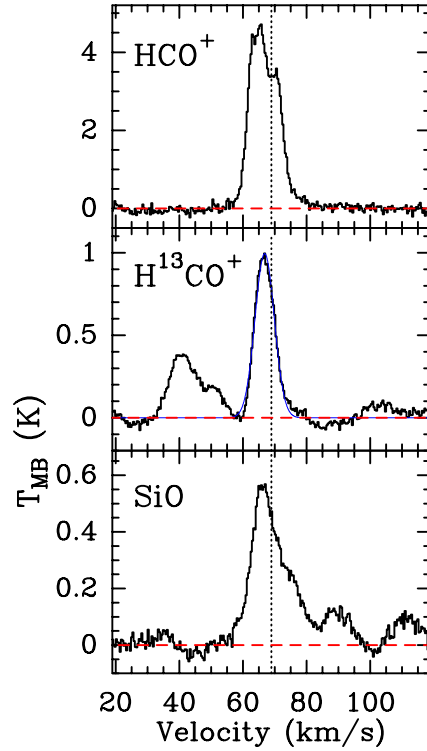
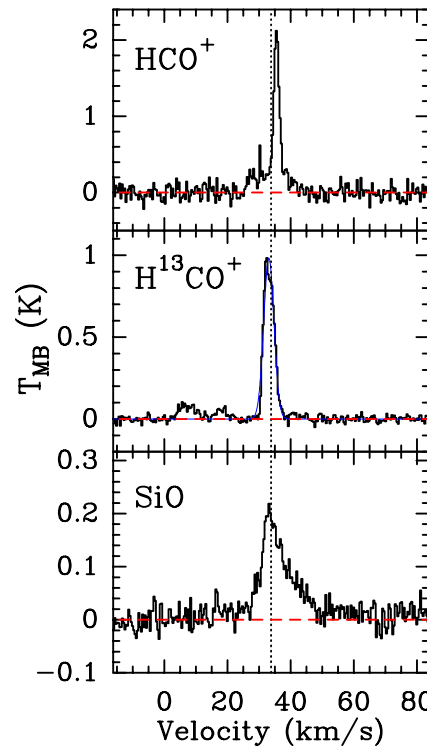## Appendix D: Spectral profiles at the SiO(4-3), H¹³CO⁺(2-1), and HCO⁺(2-1) lines
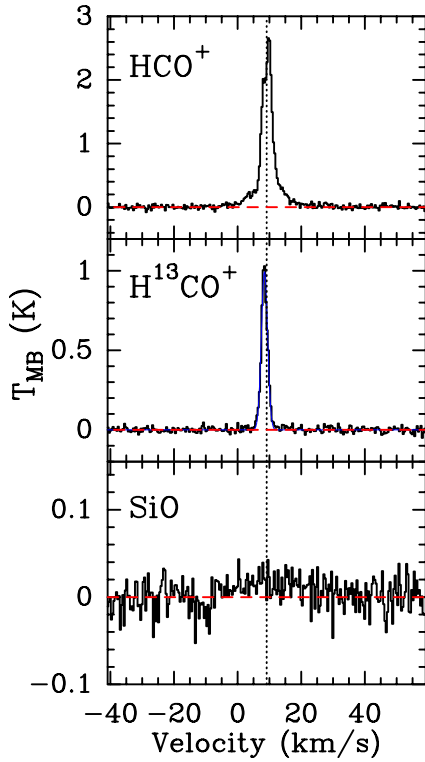
Fig. D.1. Spectral profiles for source HC01, Group C. The red dotted line is at FWZP, and the blue line in the H¹³CO⁺ panel shows the Gaussian fit.
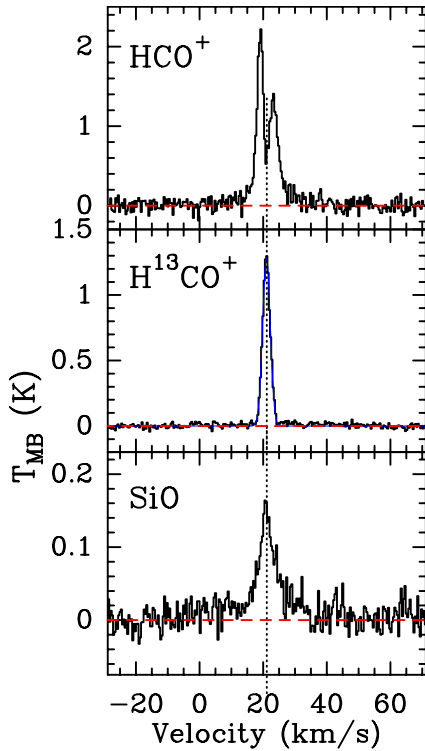
Fig. D.2. Spectral profiles for source HC03, Group B. The red dotted line is at FWZP, and the blue line in the H¹³CO⁺ panel shows the Gaussian fit.
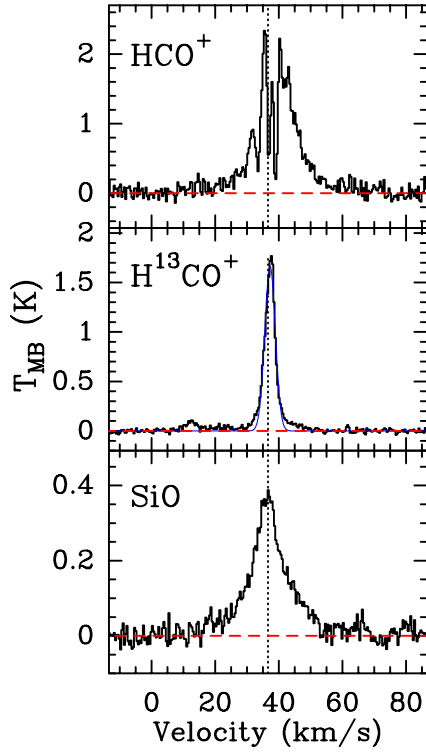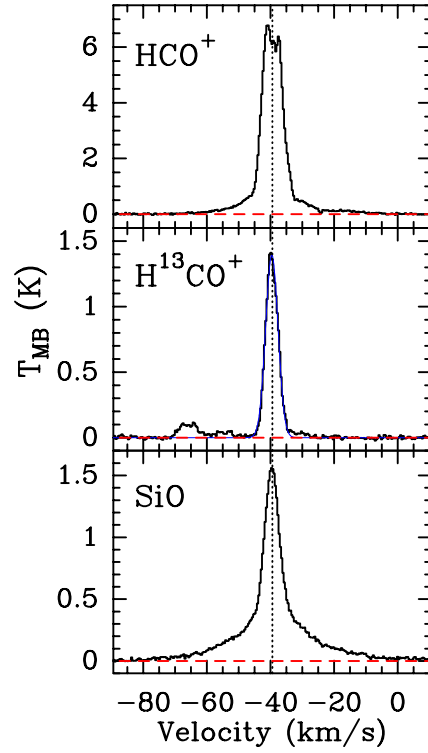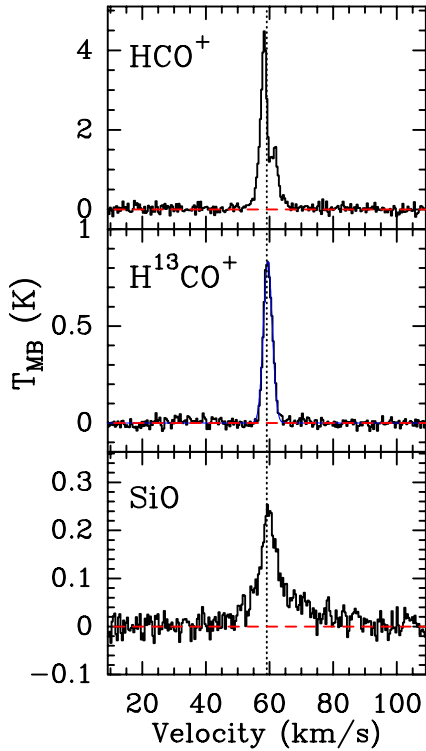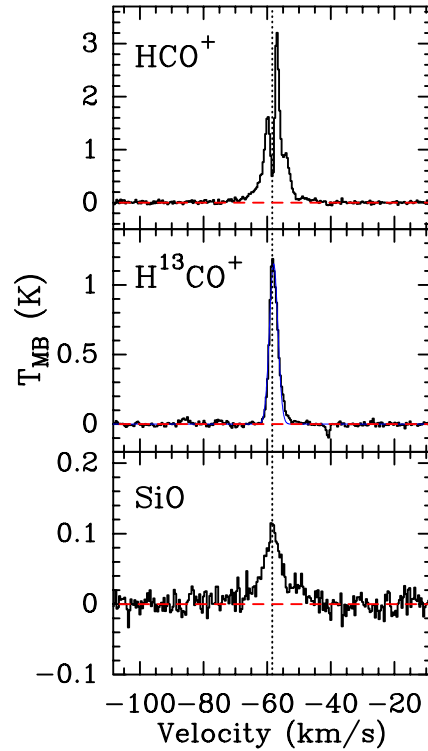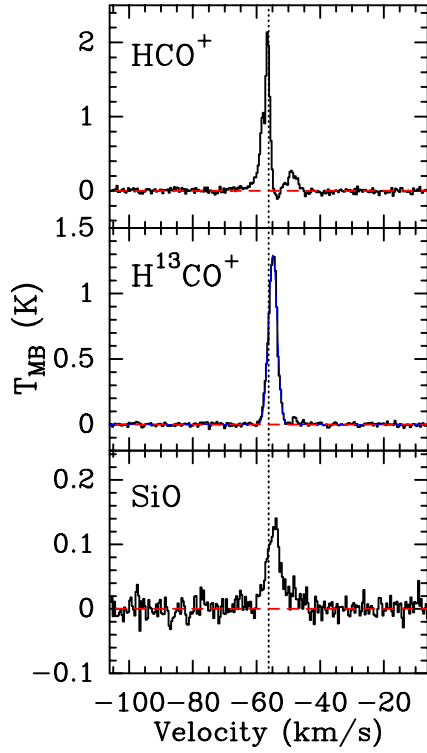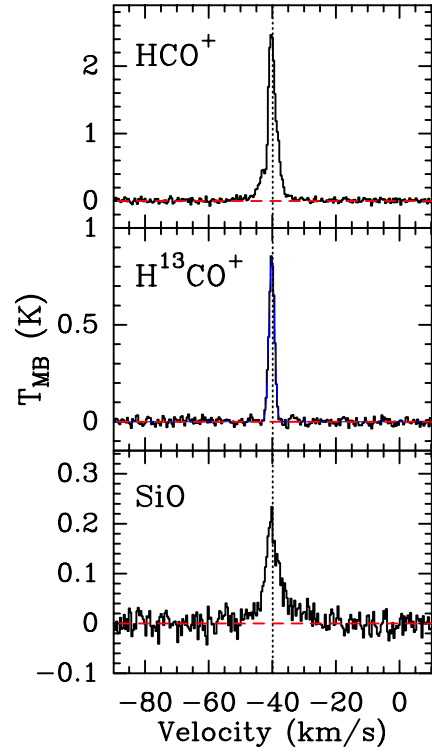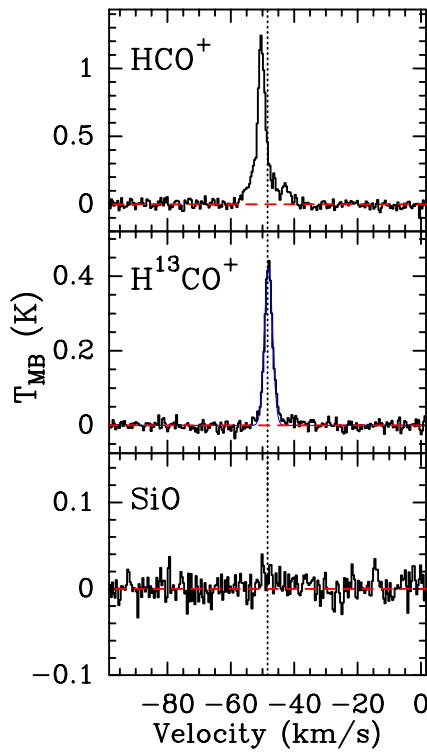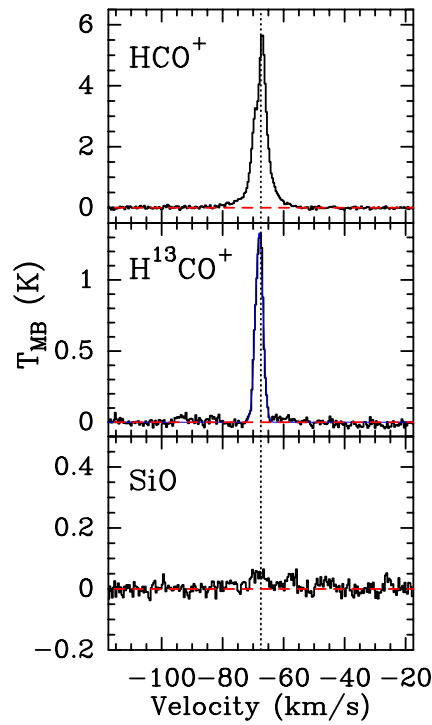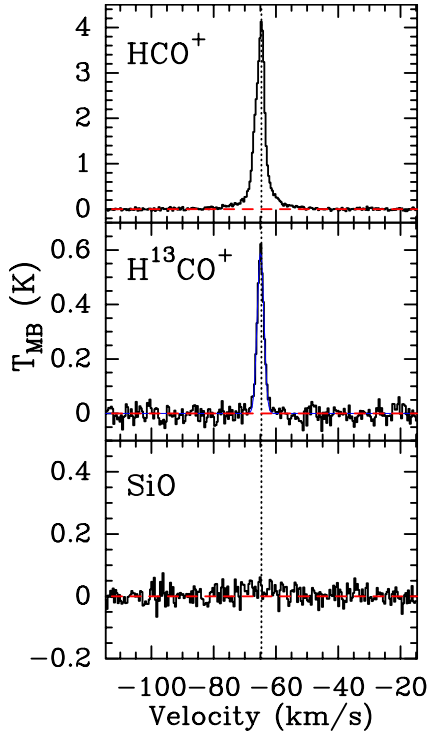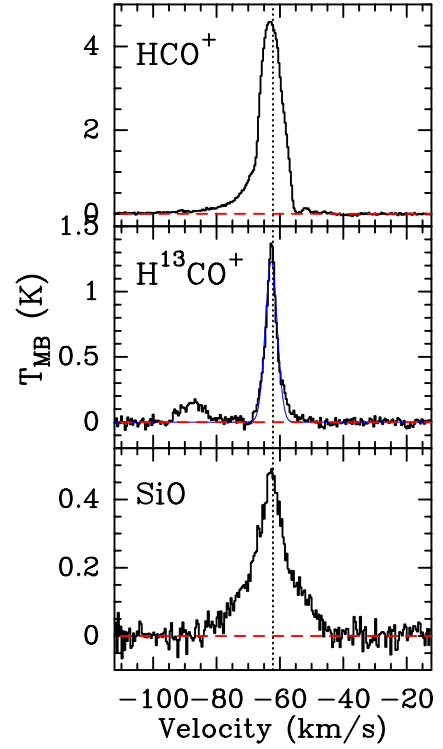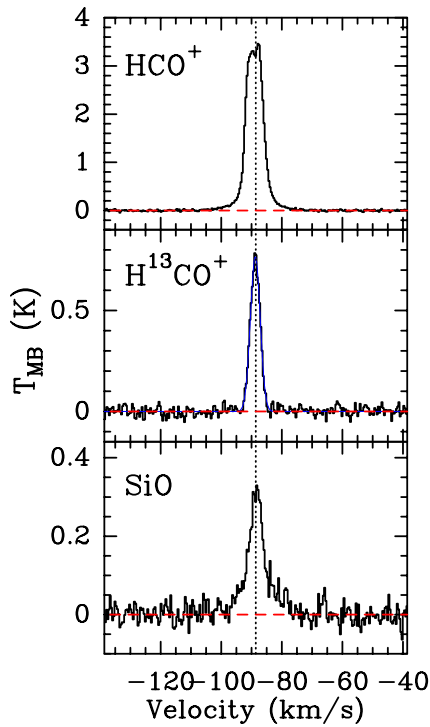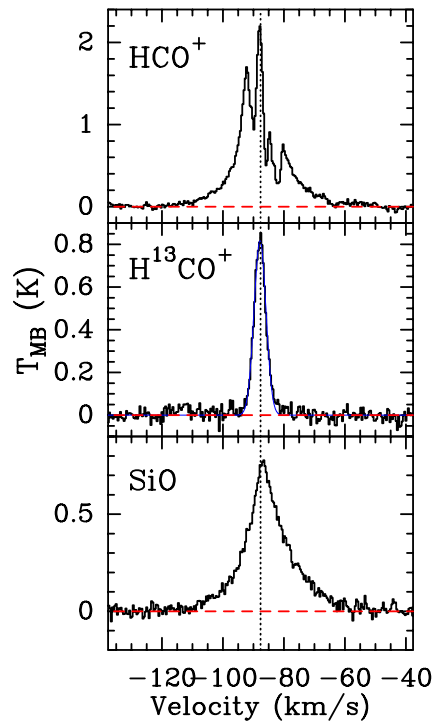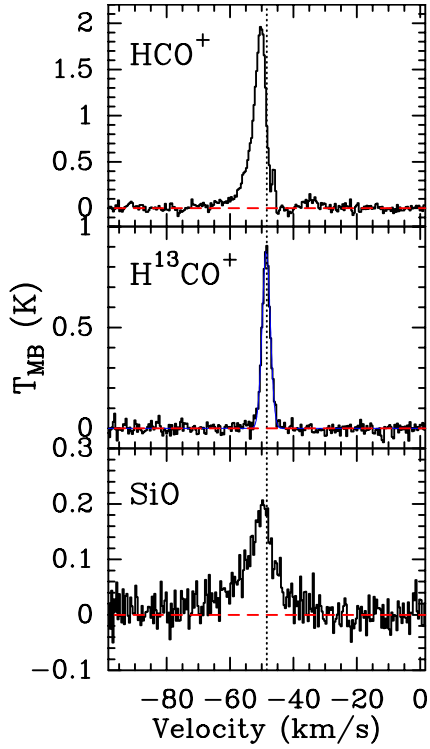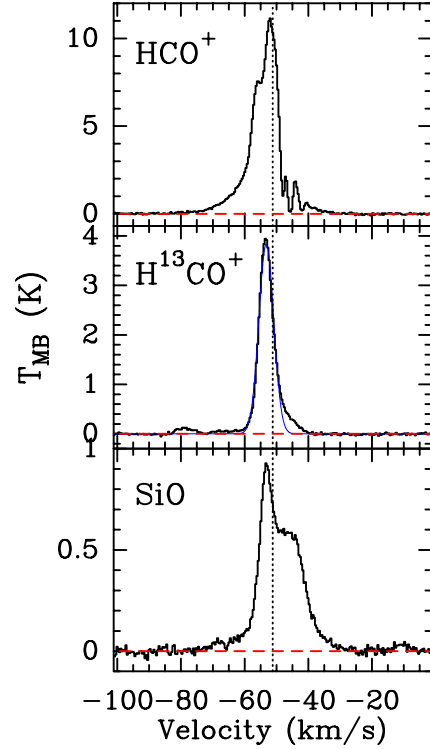

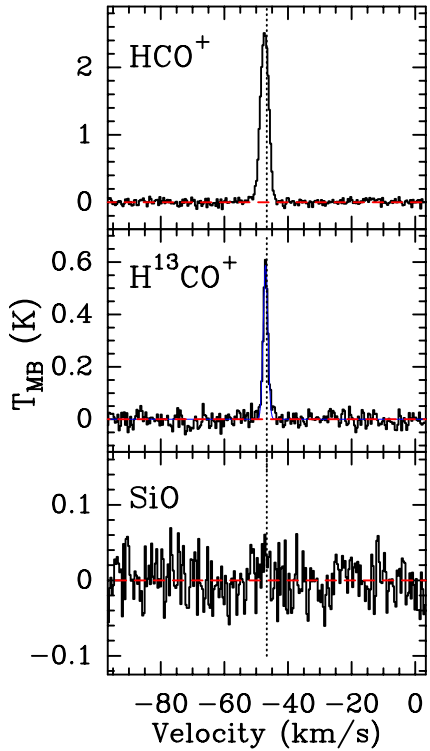**Fig. D.3.** Spectral profiles for source HC04, Group B. The red dotted line is at FWZP, and the blue line in the H¹³CO⁺ panel shows the Gaussian fit.

Fig. D.4. Spectral profiles for source HC05, Group B. The red dotted line is at FWZP, and the blue line in the H¹³CO⁺ panel shows the Gaussian fit.

Fig. D.5. Spectral profiles for source HC06, Group B. The red dotted line is at FWZP, and the blue line in the H^{13}CO$^+$ panel shows the Gaussian fit.
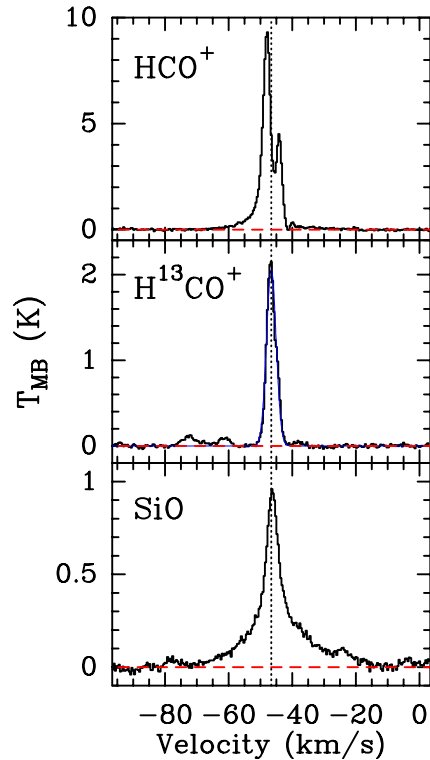

Fig. D.7. Spectral profiles for source HC08, Group A. The red dotted line is at FWZP, and the blue line in the H^{13}CO$^+$ panel shows the Gaussian fit.
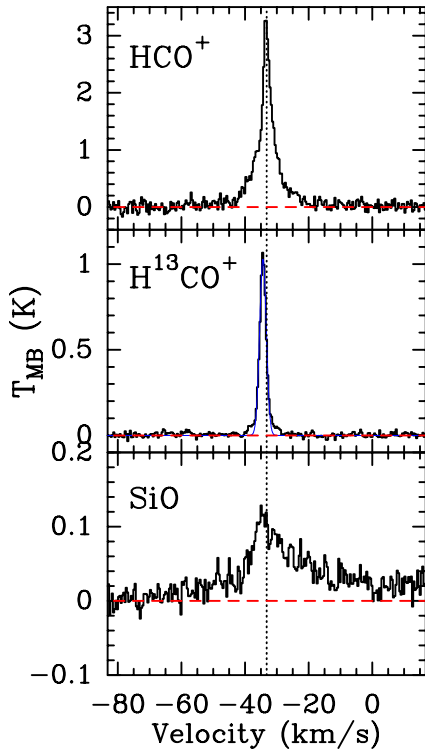

Fig. D.6. Spectral profiles for source HC07, Group B. The red dotted line is at FWZP, and the blue line in the H^{13}CO$^+$ panel shows the Gaussian fit.

Fig. D.8. Spectral profiles for source HC09, Group B. The red dotted line is at FWZP, and the blue line in the H^{13}CO$^+$ panel shows the Gaussian fit.

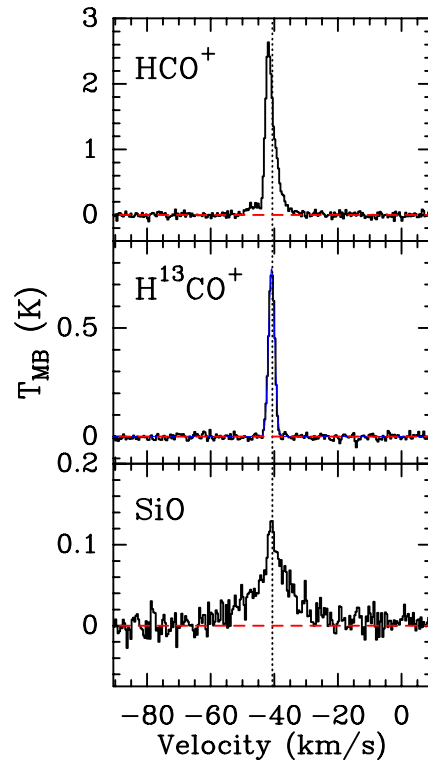**Fig. D.9.** Spectral profiles for source HC10, Group B. The red dotted line is at FWZP, and the blue line in the $H^{13}CO^+$ panel shows the Gaussian fit.

Fig. D.11. Spectral profiles for source HC12, Group B. The red dotted line is at FWZP, and the blue line in the $H^{13}CO^+$ panel shows the Gaussian fit.

Fig. D.10. Spectral profiles for source HC11, Group C. The red dotted line is at FWZP, and the blue line in the $H^{13}CO^+$ panel shows the Gaussian fit.

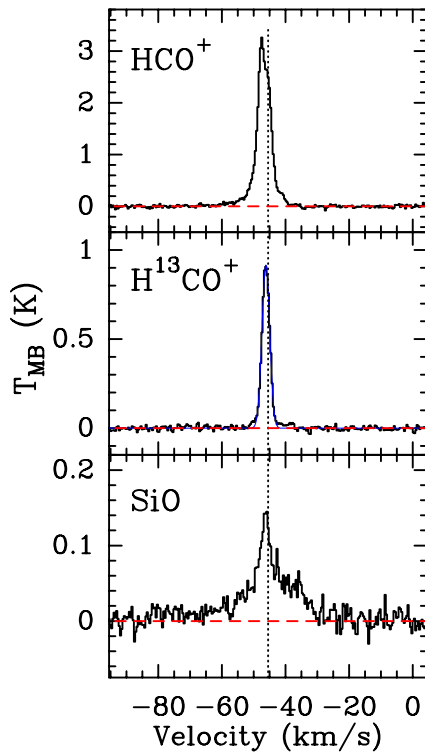**Fig. D.12.** Spectral profiles for source HC13, Group C. The red dotted line is at FWZP, and the blue line in the $H^{13}CO^+$ panel shows the Gaussian fit.

Fig. D.13. Spectral profiles for source HC14, Group C. The red dotted line is at FWZP, and the blue line in the H^{13}CO$^+$ panel shows the Gaussian fit.

Fig. D.15. Spectral profiles for source HC16, Group A. The red dotted line is at FWZP, and the blue line in the H^{13}CO$^+$ panel shows the Gaussian fit.

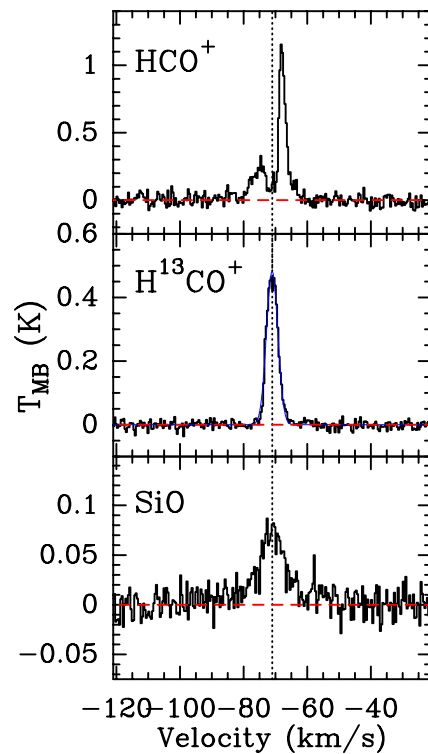**Fig. D.14.** Spectral profiles for source HC15, Group B. The red dotted line is at FWZP, and the blue line in the H^{13}CO$^+$ panel shows the Gaussian fit.

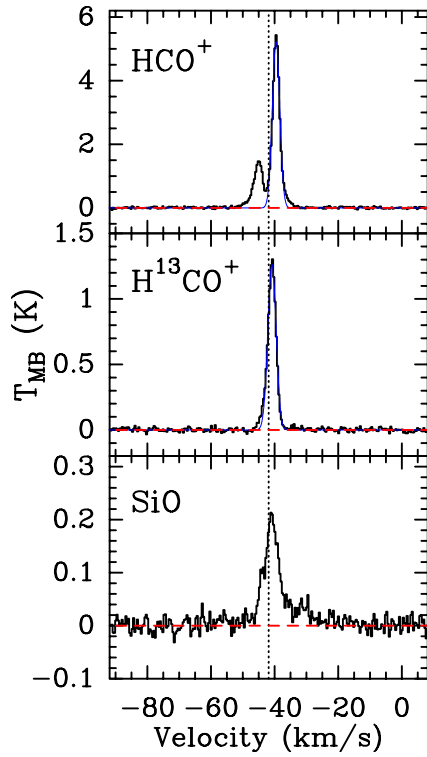**Fig. D.16.** Spectral profiles for source HC17, Group A. The red dotted line is at FWZP, and the blue line in the H^{13}CO$^+$ panel shows the Gaussian fit.

Fig. D.17. Spectral profiles for source HC18, Group A. The red dotted line is at FWZP, and the blue line in the H^{13}CO$^+$ panel shows the Gaussian fit.

Fig. D.19. Spectral profiles for source HC20, Group A. The red dotted line is at FWZP, and the blue line in the H^{13}CO$^+$ panel shows the Gaussian fit.
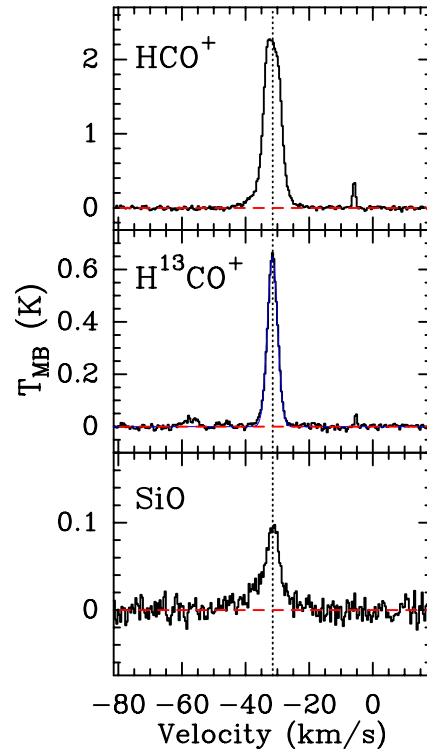

Fig. D.18. Spectral profiles for source HC19, Group C. The red dotted line is at FWZP, and the blue line in the H^{13}CO$^+$ panel shows the Gaussian fit.

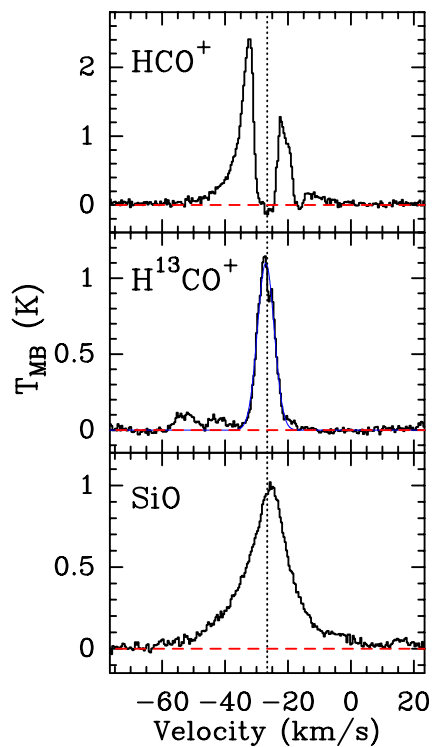**Fig. D.20.** Spectral profiles for source HC21, Group A. The red dotted line is at FWZP, and the blue line in the H^{13}CO$^+$ panel shows the Gaussian fit.

Fig. D.21. Spectral profiles for source HC22, Group A. The red dotted line is at FWZP, and the blue line in the $H^{13}CO^+$ panel shows the Gaussian fit.

Fig. D.23. Spectral profiles for source HC24, Group B. The red dotted line is at FWZP, and the blue line in the $H^{13}CO^+$ panel shows the Gaussian fit.
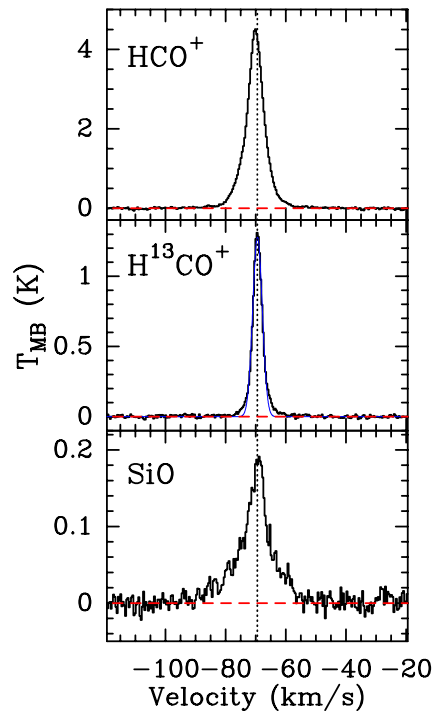

Fig. D.22. Spectral profiles for source HC23, Group B. The red dotted line is at FWZP, and the blue line in the $H^{13}CO^+$ panel shows the Gaussian fit.

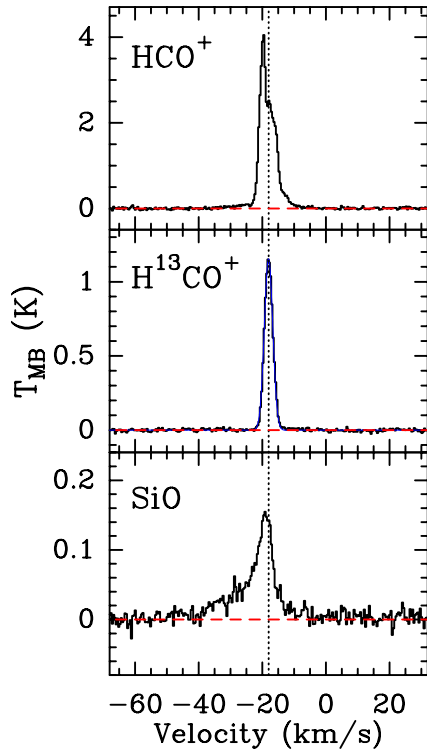**Fig. D.24.** Spectral profiles for source HC25, Group B. The red dotted line is at FWZP, and the blue line in the $H^{13}CO^+$ panel shows the Gaussian fit.

Fig. D.25. Spectral profiles for source HC26, Group B. The red dotted line is at FWZP, and the blue line in the H^{13}CO$^+$ panel shows the Gaussian fit.
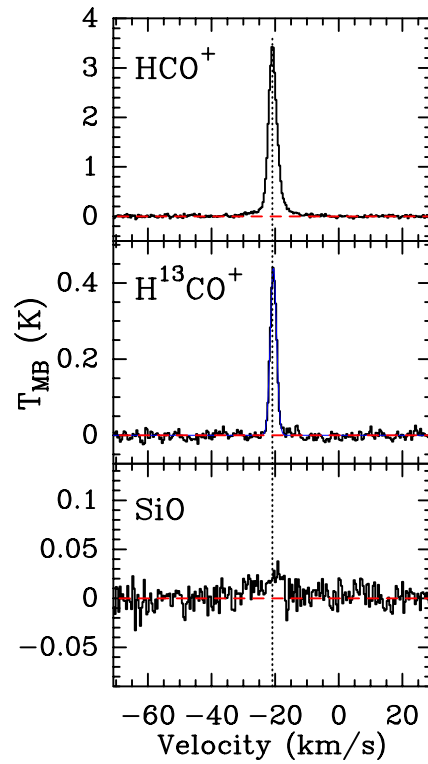
Fig. D.27. Spectral profiles for source HC28, Group B. The red dotted line is at FWZP, and the blue line in the H^{13}CO$^+$ panel shows the Gaussian fit.

Fig. D.26. Spectral profiles for source HC27, Group B. The red dotted line is at FWZP, and the blue line in the H^{13}CO$^+$ panel shows the Gaussian fit.
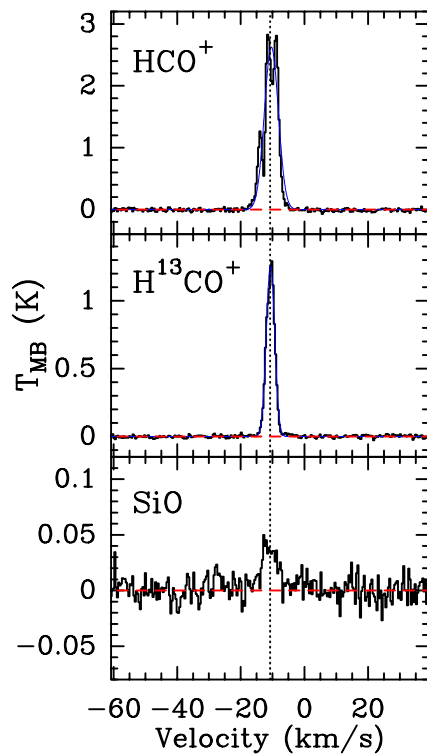
Fig. D.28. Spectral profiles for source HC29, Group A. The red dotted line is at FWZP, and the blue line in the H^{13}CO$^+$ panel shows the Gaussian fit.

Fig. D.29. Spectral profiles for source HC30, Group B. The red dotted line is at FWZP, and the blue line in the H^{13}CO$^+$ panel shows the Gaussian fit.

Fig. D.31. Spectral profiles for source HC32, Group C. The red dotted line is at FWZP, and the blue line in the H^{13}CO$^+$ panel shows the Gaussian fit.

Fig. D.30. Spectral profiles for source HC31, Group C. The red dotted line is at FWZP, and the blue line in the H^{13}CO$^+$ panel shows the Gaussian fit.